Solid Earth
Discussions

Mapping the fracture network in the Lilstock pavement, Bristol Channel, UK: manual versus automatic

Christopher Weismüller[1], Rahul Prabhakaran[2,3], Martijn Passchier[4], Janos L. Urai[4], Giovanni Bertotti[2], Klaus Reicherter[1]

5   [1] Neotectonics and Natural Hazards, RWTH Aachen University, Aachen, Germany
[2] Department of Geoscience and Engineering, Delft University of Technology, Delft, the Netherlands
[3] Department of Mechanical Engineering, Eindhoven University of Technology, the Netherlands
[4] Structural Geology, Tectonics and Geomechanics, RWTH Aachen University, Aachen, Germany

10   *Correspondence to* Christopher Weismüller (c.weismueller@nug.rwth-aachen.de)

Abstract. The 100,000 m² wave-cut pavement in the Bristol Channel near Lilstock, UK, is a world-class outcrop, perfectly exposing a very large fracture network in several thin limestone layers. We present an analysis based on manual interpretation of fracture generations in selected domains and compare this with automated fracture tracing.

15   Our dataset of high-resolution aerial photographs of the complete outcrop was acquired by unmanned aerial vehicle, using a survey altitude optimized to resolve all fractures. We map fractures and identify fracture generations based on abutting and overprinting criteria and present the fracture networks of five selected representative domains. Each domain is also mapped automatically using ridge detection based on the complex shearlet transform method. The automatic fracture detection technique provides results close to the manually

20   mapped fracture networks, however, with a bias towards closely spaced Y over X nodes. The assignment of fractures into generations cannot be done automatically yet. Generations one and two are long fractures that traverse our domains. Generation three is only present in the southwestern domains. Generation four follows an ENE-WSW striking trend, is sub-orthogonal to generations one and two and abuts on them and generation 3 if present. Generations five is the youngest fracture set with diffuse orientation, creating polygonal patterns by

25   abutting on all older fracture generations. Our mapping results show that the northeastern domains only contain four fracture generations, thus the five generations of the outcrop identified in the southwestern domains are either not all present in each of the five domains or vary locally in their geometry, preventing the interpreter to link the fractures to their respective generation over several spatially separate mapping domains. The domains have different P_{21} fracture intensities which is lowest in the NE with 7.31 m/m² and highest in the SW with 10.01 m/m²,

30   coinciding with different fracture orientations, and distributions of abutting relationships. Each domain has slightly different fracture network characteristics. The network analysis shows that connectivity increases, depending on the evolving fracture generations.

1. Introduction

Recent technological advances allow us to collect large amounts of remote sensing and outcrop data, e.g. using
35   LiDAR, unmanned aerial vehicles (UAV), and structure from motion (SfM) tools (Bemis et al., 2014; Bisdom et al., 2017; Hansman and Ring, 2019; Müller et al., 2017; Niethammer et al., 2012; Vasuki et al., 2014; Weismüller et al., 2019; Westoby et al., 2012). These high-resolution datasets can be acquired in short periods of time, optimizing resolution and enabling the detailed digitalization of km-scale outcrops in sub-cm resolution. The mapping and interpretation of features in the datasets is time-consuming because of the very large areas available
40   which must be mostly interpreted manually. Automated tools can aid during the process, but do not yet match the

quality and reliability of manual interpretations and thus must be used with care (Duelis Viana et al., 2016; Vasuki et al., 2014).

Several sampling techniques have been developed to extract data on fracture sets that do not necessarily require a complete mapping of the whole area, e.g. line sampling (Priest and Hudson, 1981), polygon or areal sampling (Wu 45 and D. Pollard, 1995), circular scanline sampling (Mauldon et al., 2001; Rohrbaugh et al., 2002; Watkins et al., 2015) or rectangular window sampling (Pahl, 1981).

In this work we use a UAV to collect aerial images of the fractured limestone at the Lilstock coast in the Bristol Channel, UK. Sample pictures and tests from varying height in combination with ground-truthing show that we resolve all visible mode I barren fractures in the pavement, which are the target of this study. With the right 50 compromise between flight altitude and resolution, we photographed the whole outcrop of 400x150 m within two days, creating a set of raw images depicting a fracture network which is too large to be manually interpreted. In a companion paper (Passchier et al., XXXX) we present a fracture mapping study, and propose criteria for identifying the different generations of fractures. Our aim in this study is to provide a complete interpretation and fracture network analysis of the selected sub-areas of the outcrop, providing a benchmark of our analyses. We 55 hand-interpret several domains and use them as basis for supervised automatic tracing to create a large fracture dataset. We present our interpretation of several fracture generations in the selected areas to review the evolution of the fracture network in time steps, using topological branch and node analysis (e.g. Dimmen et al., 2017; Morley and Nixon, 2016; Nyberg et al., 2018; Procter and Sanderson, 2018; Sanderson and Nixon, 2015). By comparing these areas, we give further estimates on the spatial variation within the larger fracture network.

60 ## 2. Study area

2.1 Geology

The study site is a wave-cut platform on the southern coast of the Bristol Channel in Somerset (Fig. 1a), close to the hamlet Lilstock. The outcrop exposes joints, faults, and fractures in a lower Jurassic sedimentary sequence of bituminous shale, marl, and limestone (Fig. 1b). The site is renowned among structural geologists and the subject 65 of various publications studying faults, fractures, fracture relationships, or basin inversion (Crider and Peacock, 2004; Dart et al., 1995; Gillespie et al., 2011; Glen et al., 2005; Peacock et al., 2018; Peacock and Sanderson, 1991; Procter and Sanderson, 2018; Rawnsley et al., 1998). We focus on a single fractured limestone layer that has been previously referred to as "the bench" (Loosveld and Franssen, 1992) or "Block 5" (Engelder and Peacock, 2001).

70 Several tectonic phases are inferred from the structures found in the Bristol Channel basin, starting with two events of N-S extension, in the Jurassic to Early Cretaceous and Late Cretaceous to Oligocene, followed by the Alpine N-S contraction from the late Oligocene to Miocene and the progressive relaxation during the Late or post-Miocene (Rawnsley et al., 1998). These events are recorded as conjugate E-W striking normal faults (Brooks et al., 1988) caused by the extension and conjugate strike slip faults along with inverted normal faults which resulted from the 75 subsequent compression (Dart et al., 1995; Glen et al., 2005; Kelly et al., 1999; Nemčok et al., 1995). The scope of this study are mode I fractures in the limestone layers, which have been studied by Agheshlui et al. (2018), Azizmohammadi and Matthäi (2017), Belayneh et al. (2006a, 2006b), Belayneh and Cosgrove (2004), Engelder and Peacock (2001), Gillespie et al. (2011), Loosveld and Franssen (1992), Matthäi et al. (2007), Matthäi and Belayneh (2004), and Peacock and Sanderson (1991, 1994, 1995). According to Engelder and Peacock (2001),

80 minor tectonic events post-date the inversion and resulted in the jointing of the limestone: the first joint set of the Bristol Channel was possibly caused by a stress field consistent with second Alpine event during the late Oligocene to Miocene (Rawnsley et al., 1998). A second phase of jointing that follows a propagation sequence consistent with an anticlockwise shift (NW-SE to NE-SW) of the regional maximum horizontal stress (Loosveld and Franssen, 1992), a period of E-W compression (Hancock, 1969) and unfilled jointing caused by basin-wide

85 relaxation of the Alpine compression (Rawnsley et al., 1998). Engelder and Peacock (2001) further point out that the youngest joint set shows a correlation with the contemporary tectonic stress field (Bevan and Hancock, 1986; Hancock and Engelder, 1989), and that the youngest NW-striking joint sets in NW Europe could be caused by exhumation in a late stage Alpine stress field (Hancock and Engelder, 1989).

2.2 Data set

90

We selected five 140 m² large rectangular domains to be mapped and interpreted, both manually and automatically, from the generated ortho-mosaics that have a spatial resolution of ~ 1 cm/pixel. Three domains are located on the south-western part of "the bench", referred to as SW1, SW2, and SW3 (from W to E), and domains on the north-eastern part, referred to as NE1 and NE 2 (from NW to SE) (Fig.1b). The reasoning behind the selection of the

95 specific regions are:

i.   all domains are within a single fractured limestone layer "the bench", allowing us to compare the spatial variation of the fracture network within the layer,

ii.   fractures in "the bench" have erosion-enhanced aperture and hence are easily detected in UAV-

100   photographs,

iii. "the bench" offers the largest exposure of a sub-horizontal single layer,

iv.   a qualitative review indicated that the fracture network complexity changes over short distances in the southwestern part of "the bench",

v.   fractures show a distinct radial pattern in the NE and our domains were chosen to partly overlap with the

105   area studied in Gillespie et al. (2011), allowing a comparison of the results.

The size of the domains (140 m² each) has been chosen in to be as large as possible, to prevent over-censoring of longer fractures, while still allow manual mapping in an appropriate amount of time.

3. Methods

110   ### 3.1 UAV

We used a DJI Phantom 4 UAV with a 12 MP camera to capture several sets of overlapping photographs of the pavement from an orthogonal perspective to create ortho-rectified mosaics. These mosaics were used as a raster layer for detailed mapping of the fracture network. To optimize the quality of the raw image data, the aerial photographs were acquired on days with suitable weather conditions: low wind velocities, no rain, sunny

115   conditions with almost clear skies and warm temperature, that lead to the complete evaporation of the seawater on the surface, but not in the cavities of the fractures, further increasing the contrast between fracture and matrix. Because the near-flat topography does not cast shadows, sunny conditions in combination with the contrast due to

the wet fractures are superior to the typically recommended cloudy skies that usually result in a better image quality as diffuse light casts fewer shadows with lower dynamic range. The setting at the coast of the Bristol Channel necessitates data acquisition at low tide, since most of the pavement is covered by the sea during high tide and the outcrop is washed clean but dries quickly on a clear, warm day. To optimize the volume of data acquisition during a single day, we undertook as many flights as possible during low tide in the morning and again in the afternoon. Apart from the cliff, the coast is flat without major obstacles, enabling us to automate the UAV mapping procedure by using Pix4Dcapture to pre-generate flight routes for the UAV. The automation provides better control on the degree of overlap between each photograph. We used settings of at least 80% frontlap and 60% sidelap with vertically downwards facing camera, resulting in 8-9 perspectives per point in the center of our models that are adequate to create a 2D map of a low topography surface.

To identify the optimum between flight altitude and resolution, we took sample photographs starting at 7 m up to 100 m (Fig. 2). We evaluated the spatial resolution in the photographs with respect to fractures we can identify in the outcrop. An altitude ranging between 20 - 30 m offers the best balance between flight altitude and thus being able to cover larger areas in shorter time and a spatial resolution depicting all fractures in the photographs. Photographs taken from an altitude of 100 m (Fig. 2a) resolve only the larger fractures, which is possible because of the high contrast between fracture and rock (cf. Gillespie et al., 2011). We used the SfM photogrammetry software Agisoft PhotoScan to match the photographs, calculate camera perspectives, and create dense point clouds. Using the point clouds, digital elevation models (DEMs) were calculated achieving resolutions < 2.3 cm/pixel for flight altitudes below 25 m above ground. These DEMs were used as reference surfaces for the calculation of the ortho-mosaics with resolutions ~ 1 cm/pixel respectively. To further test our survey altitude (Fig. 2) we additionally covered selected areas from 10 m flight altitude, resulting in DEMs of 8 mm/pix resolutions and ortho-mosaics with 4 mm/pix. No other fractures can be identified in these models which have not been resolved from flight altitudes of 25 m, thus we opted for higher altitudes to reduce survey time/battery and data volume. An overview (Fig. 1b) has been created from photographs taken from a flight altitude of 100 m, showing structures of larger scale, but is not detailed enough to accurately map fractures. The spatial resolution in the ortho-mosaic from 100 m is 4.21 cm/pix, which is slightly better than the 5 cm/pixel achieved by Gillespie et al. (2011), (their figures 8 and 9), who used a large-scale camera for an aerial photographic survey by airplane.

Since we focus on the 2D geometry of the fracture networks, we were able to omit the placement of ground control points to increase the geo-referencing accuracy. The onboard GPS receiver of our UAV allows absolute horizontal positioning in the range of few meters and we only refer to the relative not absolute positioning. Quality control and ground truthing were done by field observation and measurements on objects of known size in our models.

3.2 Fracture trace mapping

It is not possible to manually map all fractures on the whole outcrop within reasonable time; thus, an automatic fracture mapping technique seems obvious. However, the reliability along with the strengths and weaknesses of automatic fracture detection must be addressed first. To do so, we use both techniques for the same domains, allowing a direct comparison of the results. This helps us to identify potential human bias (e.g. Andrews et al., 2019; Peacock et al., 2019) and gives us a measure of quality of the automatic fracture detection technique, which then can be optimized to map the whole outcrop in future work.

In the manual approach, fractures are traced as polylines from tip to tip. We traced the widely eroded fractures along their medial axis creating as few vertices as possible, while still maintaining the original fracture geometry.

Abutting fractures were mapped as polylines and snapped at the abutting intersections. Snapping is not necessary for cross-cutting fractures, but it is for intersections where a younger fracture converges to an existing junction.

160   An approach to semi-automatically map this outcrop has been published by Gillespie et al. (2011), who used ant tracking on a lower resolution dataset, resulting in a good overview of the fracture geometry, but incomplete fracture detection (their Fig. 9) which is insufficient for a detailed analysis of crosscutting relationships. To overcome these limitations, we use the technique presented in Prabhakaran et al. (2019), that allows detailed detection of fractures in our data. The automated trace extraction is based on ridge detection using the complex

165   shearlet transform method as described by Reisenhofer et al. (2016) and extended to fracture trace extraction from drone photogrammetry by Prabhakaran et al. (2019). The automatic processing consists of serial image processing steps applied to the UAV-images, including ridge ensemble computation, segmentation, skeletonization, and polyline fitting (Fig. 3). The automatic trace extraction requires a selection of parameters pertaining to the shearlet systems. For the Lilstock dataset, we chose a set of shearlet systems that capture fractures of multiple scales and

170   applied it to all image tiles. Subsequently, for each image tile, the intensity threshold was adjusted to convert ridge ensemble maps into binarized images by visual comparison with the source image. Such a step was necessary owing to the spatially varying fracturing intensity.

3.3 Network analysis

175   To analyze the fracture networks, we chose a sampling strategy comparable to the polygon sampling explained in Nyberg et al. (2018) by completely analyzing the mapped domains. This allows us to analyze the domains entirely and identify possible spatial heterogeneities. We used ArcGIS as main platform in combination with the NetworkGT plugin (Nyberg et al., 2018). The ArcGIS environment enables us to measure fracture length, calculate fracture and segment sinuosity, and measure strike directions. 2D fracture networks may be described in terms of

180   nodes and edges that constitute a spatial graph. The nodes are classified in terms of node degree, i.e., the number of edges that pass through it, and the edges are classified based on the type of branches. Sanderson and Nixon (2015) specify three node types, isolated (I), abutting (Y), and crosscutting (X) whose relative proportions define the topology of the graph. In our interpretations, the nodes of fractures clipped by the boundary of the selected area are classified as end nodes (E). The fracture segments connecting the nodes and referred to as branches, that

185   may be classified into three types. The branch types are I – I when both nodes at the branch tips are I-nodes, C-I when connected at one tip (via an abutting or crosscutting node) but isolated at the other, and C-C when both tips end at a Y or X node. To apply the topological analysis tools provided by the NetworkGT plugin (Nyberg et al., 2018), we split the manually traced fractures into segments between intersections. This step is not necessary for the automatically generated traces that are already segmented as output from the technique of Prabhakaran et al.

190   (2019). NetworkGT only supports nodes of the types I, Y, and X, and nodes of higher order are returned as error nodes. These error nodes consisting of node degree greater than four, are corrected and distinguished as special cases of X nodes, where five (Penta), six (Hexa), seven (Hepta) or eight (Octa) branches intersect. The spatial join function was used to count the number of intersecting branches at the specific nodes and their classes were reassigned accordingly. Linkage to an unknown type of node yields errors in the recognition of branch

195   connectivity. These errors were corrected using SQL queries to select undefined branches to change their connectivity accordingly to their number of connected ends.

3.4 Manual classification of fractures into generations

To distinguish different generations of the manually traced fractures, we used abutting and cross cutting relationships as discussed in Peacock et al. (2018) aided by general fracture attributes such as length and strike. The interpretation of fracture generations on this dataset along with detailed rules for the classification of generations is presented on a larger scale by Passchier et al. (XXXX) and therefore kept briefly within this section, focusing on the application in our domains. Fracture generations were assigned following the criteria below:

Gen. 1: Longest fractures that traverse through the study areas. Absolute orientations are not used as criterion because they are not reliable in converging patterns as present in the NE of "the bench".

Gen. 2: Subparallel orientation to gen. 1, shorter in length and abuts on to gen. 1.

Gen. 3: Shorter than gen. 1 and 2, oriented at a sharp acute angle to gen. 1 and 2 and abuts on to them.

Gen. 4: ENE-WSW striking, sub-orthogonal to gen. 1 and 2 and abutting gen. 1 and 2, also abuts and crosscuts gen. 3

Gen. 5: Shortest with diffuse orientation and abuts all other generations sub-orthogonally, creating polygonal shapes

Distinguishing generations 1 and 2 by length is not possible for all fractures because large parts extend outside of our selected domains. Thus, we decided to adopt the interpretation of Passchier et al. (XXXX) for fractures of generations 1 and 2 in the southwestern domains. A fracture set analogous to generation (gen.) 3 in the SW could not be identified in the domains in the NE. Our interpretation of fracture generations is in line with the four main joint sets introduced in Rawnsley et al. (1998) for the northeastern areas. Further interpretations of the different sets of joints include (Belayneh and Cosgrove, 2004; Engelder and Peacock, 2001; Loosveld and Franssen, 1992), who interpreted up to six generations of joints in the Lilstock pavement.

4. Results

4.1 Fracture traces

We traced fractures in five different domains of 140 m² each (Fig. 1b) manually and automatically and present the resulting trace maps as P_{21} fracture intensity plots (Dershowitz and Herda, 1992) in Fig.4. The difference between the manual and automatic interpretations is depicted as a spatial map of as P_{21} fracture intensity difference in the supplement S1. Despite a slightly larger number of fracture segments in the automatically generated code compared to the manual interpretation, the resulting plots are very similar. The automated extraction results in traces segmented at the fracture intersection nodes. The number of traces is therefore higher than the number of fracture traces as would be described by an interpreter mapping complete fractures. However, these segmented traces already resemble the branches as used for the network analysis and have been processed to represent branches and nodes (Figs. 5 and 6). Further analyses of the automatically generated networks show that the P_{21} fracturing intensity in higher in the SW study area compared to the NE and within the SW study areas is highest in SW2 (Table 1).

A quantitative comparison of the interpreted fractures from the five domains shows that the number and mean lengths within the south-western domains and NE1 is similar, but clearly differ from NE2 (Table 1, Fig. 7): in the

south-western domains and NE1 between 8184 and 8548 branches were counted with mean lengths between 0.15 m and 0.17 m, while NE2 only has 4831 branches which are therefore longer with a mean length of 0.21 m. The trend of NE2 having longer branches than the other domains is consistent over the 25%, 50% and 75% quartiles. Minimum lengths in all domains are < 1 cm, thus cannot be accurately resolved in our orthorectified mosaics. This

240   trend is not present in the maximum lengths of the branches, which are largest in SW2 (0.97) and shortest in NE1 (0.57). The covariance is relatively similar in all domains, ranging from the lowest (0.56) in NE1 to the highest (0.7) in SW1. The kurtosis in all domains is positive and are closest to that of a half normal distribution (3) in SW1 with a decreasing trend towards the E. All domains show a positive skewness with a decreasing trend towards the E as well, indicating that the branch distribution in the eastern domains is closer to a symmetric one, while the

245   distributions in the W are more asymmetric with a tail towards longer branches. The cumulative length distribution plots and the plots of log normal standard deviation (Fig. 7) show that our dataset resembles the characteristic negative power law associated with fracture traces. The resulting traces generated by the automatic technique are segmented, thus only the final cumulative network development can be analyzed. This is the case because the correct identification of abutting and crosscutting relationships is a prerequisite to identify age relationships and

250   requires one to review the complete fractures, not just segments. The resulting networks depicted as branches and nodes are presented in Fig. 5 for the domains in the SW and Fig. 6 for the domains in the NE, also showing that all visible fractures have been identified successfully. The node topology statistics indicate that the network is well connected with a relatively small proportion of isolated nodes with the system dominated by abutting (Y) nodes (Table 2 and compare with Fig.18). Isolated nodes are few in general with decreasing numbers from W to E. The

255   number of Y nodes lies between 3919 in SW3 and 4390 in SW2 in the SW, and has both, maximum and minimum values in the northeastern domains, where NE1 has the largest number (5100) and NE2 the lowest (2517). The number of X nodes along with Penta nodes increase from SW1 towards SW3 and NE1 to NE2, with NE1 having the lowest number of X nodes of all five domains. Length weighted rose plots are depicted in Fig. 8. The rose plots depict a significant variation in the fracture strike between NE and SW regions. In the SW study areas, the fracture

260   pattern is similar in all three areas. In the NE2 study area proximal to the fault, there are two predominant fracture sets. In NE1 the same two sets persist, but the fractures acquire a polygonal pattern.

4.2 Fracture generations

Within our manual interpretation we classify the fractures into generations using the rules presented in Section 3.4. The interpreted fracture generations in the SW (Fig. 9) slightly differ from the fracture generations in the NE

265   (Fig. 10). Figures presenting the raw data next to the interpretations are provided in S2-S6. The generations in the southwestern and northeastern domains are described below.

4.2.1   Southwestern domains

The SW domains (Fig.9) include five fracture generations that differ in their distribution throughout the domains.

270   In SW1 and SW2, gen. 2 fractures are more numerous than gen. 1 fractures. In SW3, this relation is reversed. Overall, the generations 1 and 2 have similar geometry. Generation 3 is represented in all three domains with increasing presence from W (SW1) to E (SW3), coinciding with an increasing fracture intensity. Generation 4 only covers a small number of fractures in each domain, while gen. 5 is present in large numbers, abutting on all older generations and converging into existing junctions. Average values of fracture length, strike, and sinuosity for the

275 domains in the SW are presented in Table 3. To identify potential clustering of the fracture strike and length, their values have been plotted for each fracture and color coded according to the associated fracture generation. Fractures in SW1 show three clusters (Fig. 11): Fractures of gen. 1 and 2 accumulate between 90° and 120°, reaching a maximum length of 18 m. Generation 3 resembles a Gauss distribution around 80° with most fractures reaching lengths up to 2 m, but also including lengths up to a maximum of 10 m. Generation 4 plots around 60°

280 with lengths up to 3 m. Fractures associated with gen. 5 are more widely distributed, covering all strike directions with denser clusters around 0°-20°, 160°-180°, and 70°-90°, representing dominant N-S and E-W orientations. Fractures in SW2 resemble the distribution of SW1 with no obvious differences. Fracture distributions in SW3 (Fig. 11) show deviations from SW1 and SW2: the cluster with the longest fractures between 100° and 120° is dominated by gen. 1, while the respective clusters in SW1 and SW2 are interpreted as mostly gen. 2, coinciding

285 with the qualitative observations before.

4.2.2 Northeastern domains

The network in NE2 (Fig. 10) mainly consists of many gen.1 fractures that converge towards a fault in the SE, while NE1 is more balanced in respect to the presence of fracture generations. Notably, the fracture networks in the northeast lack the fractures associated with gen. 3 in the SW and differ strongly in their perceived appearance.

290 The relationship of gen. 2 and 4 is complex, as they crosscut but also abut on each other. Like the domains the SW, gen. 5 is present in both domains and abuts all older generations without a preferred strike. Averages of fracture length, strike and sinuosity for NE1 and NE2 are presented in Table 4. With some differences to the domains in the SW, fracture generations the NE are clustered as well (Fig. 12). Generation 1 is mostly present between 120° and 160° in both, NE1 and NE2, reaching almost 9 m maximum length. Generation 2 shows a wider

295 cluster in NE1 with most fractures striking between 80° and 140° and a similar distribution as gen. 1 in NE2. The cluster associated with gen.3 in the SW (Fig. 11) is not present in NE1 or NE2. Another cluster at 60° is associated with gen. 4 in NE1 and NE2, which is the same in all three areas in the SW. Generation 5 is widely spread in all directions, especially in NE1, while a maximum of gen. 5 fractures between 20° and 60° is present in NE2.

4.3 Fracture network evolution

300 To analyze the impact of the fracture generations on the overall network, their traces were split at intersections into branches and the intersections represented as nodes, to resemble the fracture networks presented for the automatic trace detection in figures 5 and 6. The results are presented for SW1 - SW3 in figures 13 – 15 and NE1 and NE2 in figures 16 and 17, showing the network evolution in time steps by adding the subsequent generation

305 in each subfigure. The following sub-sections summarize the major changes for every domain during the network evolution to guide the reader through figures 8 - 12 and tables 5 - 9.

4.3.1 SW1

The initial time step comprises three sub-parallel branches of gen. 1 fractures (Fig. 13a and Table 5). Their full

310 length falls outside the mapped area and they abut at the boundary resulting in three isolated (I – I) branches of 3 m length in average. With gen. 2 (Fig. 13b) more sub-parallel branches are added, of which a large number abut at the mapping boundary, resulting in further isolated branches and an increased average length of 4.69 m. Some

gen. 2 fractures abut at gen. 1 in acute angles, resulting in Y nodes at connected (C – C) branches. Generation 3 strikes in an angle towards gen. 1 and 2, either crosscutting the older fractures (X nodes) or abutting them (Y

315   nodes) as presented in (Fig. 13c), leading to a shorter average branch length of 0.59 m. Few fractures interpreted as gen. 3 end in I nodes. Generation 4 is sparsely represented in SW1, thus the impact on the fracture network compared to the previous time step is minor (Fig. 13d). With gen. 5 (Fig. 13e) the network becomes more spatially dense, further reducing the average branch length to 0.2 m. The fractures may abut on older generations, but also tend to join in existing junctions, leading to the development of Penta and Hexa nodes. The sinuosity slightly

320   increases from gen.1 and 2 towards gen.3. From gen.4 to gen.5, it slightly reduces again.

4.3.2   SW2

In SW2, generation 1 is represented as four fractures of which two abut on the mapping boundaries at each side and two end in I nodes (Fig. 14a and Table 6). Most gen. 2 fractures end in either I nodes or at the mapping

325   boundary but can also connect to the tips of preexisting gen.1 fractures as observed on the largest gen.1 fracture in the center (Fig. 14b). Generation 2 leads to a decrease in average (avg.) branch length from 7.98 m to 4.51 m. Generation 3 has a large impact on the network, further reducing the avg. branch length to 0.54 m due to many fractures crosscutting older generations (Fig. 14c), resulting in a sharp increase of Y and X nodes. Generation 4 has a minor impact (Fig. 14d), not significantly altering the network parameters. Generation 5 (Fig. 14e) again

330   reduces the avg. branch length to 0.2 m while reducing the number of I nodes and strongly increasing the number of Y and X nodes. The sinuosity has a consistent value of 1 during all stages of the network within this domain.

4.3.3   SW3

Compared to SW1 and SW2, gen. 1 fractures are more numerous in SW3, however, they are still not well connected

335   with most fractures ending in I or E nodes at the mapping boundary (Fig. 15a and Table 7). Generation 2 is less pronounced in this area with only a small impact on the network (Fig. 15b). The average branch length slightly increases by 0.11 m, as few long fractures are added. With the addition of gen. 3 to the network (Fig. 15c), the average branch length is reduced from 3.17 m to 0.59 m, again with a strong increase of Y and X nodes. With the addition of gen. 4 (Fig. 15d), I nodes are reduced in favor of Y and X nodes. Generation 5 (Fig. 15e) further reduces

340   the avg. length to 0.2 m with a sharp increase of Y and X nodes. The sinuosity increases slightly from gen. 1 and 2 towards gen. 3 and slightly decreases again towards gen. 4.

4.3.4   NE1

Generation 1 consists of several sub-parallel branches that mostly end in I nodes or at the mapping boundary (Fig. 16a and Table 8). Abutting fractures are sparse, as only four Y and zero X nodes are observed, leading to an

345   average branch length of 4.33 m. Generation 2 (Fig. 16b) strikes at an angle to gen. 1 leading to an increase of cross cutting and abutting nodes, that are present in almost equal numbers. Also, the number of I nodes is quadrupled. The avg. branch length is reduced to 0.79 m. With the addition of gen. 4 (Fig. 16c), the avg. branch length is further reduced to 0.68 m, accompanied by an increase of abutting (Y) and cross cutting (X) nodes. Generation 5 (Fig. 16d) further reduces the avg. branch length to 0.24 m with a strong increase of Y nodes from

350 547 to 4135 and X nodes from 229 to 705. The sinuosity increases from 1 to 1.01 during the last step of the network development.

4.3.5   NE2

In this subarea, gen. 1 is present as long subparallel branches that spread out radially from a fault outside of the
355 mapping boundary (Fig. 17a and Table 9). The branches barely abut or intersect each other or create I nodes. Most of the branches run into the mapping boundaries at opposite sides, leading to an avg. branch length of 4.14 m. Generation 2 crosscuts gen. 1 almost orthogonally (Fig. 17b) leading to an increase of Y and X nodes along with a reduced avg. branch length of 0.8 m. Generation 4 (Fig. 17c) further reduces the avg. branch length to 0.45 m, with a slight increase of X and Y nodes. At this stage, the sinuosity of the network is maximal. With the addition
360 of gen. 5 (Fig. 17d) the avg. branch length is reduced to 0.16 m along with a large additional number of Y and X nodes.

A direct comparison of the node distribution for all domains is visualized in ternary plots highlighting the changing node distribution during the network development (Fig. 18 upper). Results of the latest network state (analog to
365 gen. 1 – 5 for manually traced fractures) from the automatic trace extraction are depicted in Fig. 18 lower for a direct comparison.

5.   Discussion

5.1 Manual vs automatic tracing

The resulting branch lengths and node counts of the automatic and manual procedures are listed in Table 10. Three
370 detailed examples comparing the manual and automatic interpretations processed as branches and nodes are given in Figure 19.
Manual tracing of the fracture network is comprehensive but time-consuming. At this quality of outcrop and resolution of imaging, human bias is minor, and very similar results are produced by different interpreters. A manual interpreter's work can get quality control from another interpreter, while the reliability of the automatically
375 mapped network entirely depends on ridge detection and image post-processing parameters.
Automatic mapping is fast compared to manual mapping; however, the network needs to be checked for artifacts along with a general estimation of the reliability or capability of the method before it can be applied widely. Depending on the image processing parameters chosen, this can be a huge advantage when the automatic extraction has minimal artifacts. If the automatic extraction returns many false positives and incorrect node connections,
380 correcting them can be more time-consuming than an initially correct manual interpretation. In either case, an advantage of the automatic tracing is the ability to reproduce results solely by choosing the same parameters, while manual reproduction requires the interpreter to follow a clearly defined set of rules which can become excessive depending on the complexity of the dataset. However, using the fracture mapping code described in Prabhakaran et al. (2019), it is only possible to generate segmented networks of branches and nodes. The interpretation of
385 fractures longer than a segment between two nodes and the association to a certain generation depending on crosscutting relationships still must be done manually.

10

For the data presented in this work, the results of both techniques are very similar, as shown earlier in Fig. 4. To better highlight the dissimilarities of the traced fractures, the differences of the P_{21} analyses are presented in

390 supplement S1. P_{21} plots are expected to be higher for automatically traced fractures, because the traces are more sinuous than the manually traced ones; the automatic code generates traces based on the detected ridges, while a manual interpreter tends to trace using as few vertices as possible. Regions where P_{21} is higher for manual traces show cases where the interpreter can draw a trace based on geological knowledge and not just the presence of a ridge, e.g. thinning out or merging fracture openings where the automatic detection stops but the human interpreter

395 continues the trace, resulting in longer or more numerous traces (e.g. Fig. 19 mark 7).

Fig. 19 gives a direct comparison of the manual interpretation and automatically generated fracture networks. Increasing complexity of the fracture network causes more differences in the interpretations, mainly in the interpretation and number of nodes, while the average lengths of the branches only differ by a few centimeters (see also Table 10). The manual interpretation favors nodes of higher degree in direct comparison to the automatic

400 interpretation in most cases (Fig. 19, see also Fig. 18). The biggest difference is the higher number of Y nodes counted in the automatic network: This is caused by i) the overall larger number of fractures present in the automatic code along with ii) the bias of the code towards nodes of lower degrees. Broadly eroded fractures lead to inaccuracies when the code is tracing one of the edges instead the medial axis of the fracture. More small fractures are detected leading to a higher number of isolated nodes (Fig. 19 mark 5). In the manual interpretation,

405 these have been interpreted as erosional surface features and not fractures. Thus, the difference here highlights the importance to find the right sensitivity of the image processing parameters, as a too high sensitivity will lead to wrong positives and a too low sensitivity to false negatives. Compared to the ant-tracking method in Gillespie et al. (2011) applied to a much lower resolution (5cm/pixel) dataset, we deem our results more reliable because our spatial resolution is slightly smaller than the width of the eroded fractures, allowing is to make interpretations

410 based on features in the same scale, as it would be done directly on the outcrop.

We infer that the automatic code at this stage represents a good option to create an initial fracture trace map which only differs from a manual interpretation to a degree which is comparable to the degree of deviation by another manual interpreter. More complex tasks, like an interpretation of age relationships based on abutting and crosscutting criteria still require manual input. Based on this, future work can include the extension of the

415 automatic mapping routine to the whole outcrop and use the manual interpretations to define criteria to combine automatically mapped branches into fractures and to assign fractures to predefined generations.

5.2 Classification into fracture generations

The classification of fractures into generations requires expertise of the interpreter. Locally, several generations are possible for a single fracture. In those cases, the interpreter has to make a decision with possible human bias,

420 which is the reason for outliers in figures 11 and 12: some fractures have been assigned to a certain generation, but do not match the cluster of the associate fractures. This is possible when old fractures are reactivated and abut younger fractures or fractures interact with local features, e.g. preexisting fractures, that may lead to a fracture geometry somewhat atypical for a certain set, even though the development is simultaneous. This is visible in our data as fractures that match the distribution of the youngest generation but have been initially assigned to an older

425 generation.

For our early generations fracture length is not a reliable criterion, because the fractures can be longer than the respective dimension of our mapping domain. This circumstance highlights the impact of fracture geometry on

possible interpretations and results when selecting location and dimension of mapping domains. The strike directions in the SW (100° - 120°) and NE (120° - 160°) differ, raising the question whether these are two

430   independent sets. Considering the radial/converging pattern of gen.1, that can be observed best on a larger scale on the eastern part of "the bench", we interpret the fractures as different appearances belonging to a larger structure. The underlying reason for this interpretation is that fractures associated to a structure like this can form simultaneously but in different directions. Thus, one criterion cannot rule out the other in this special case.

In the southwestern domains generations 1 and 2 are very similar in length and strike and can only be distinguished

435   when gen.2 fractures bend at the tips and abut on gen.1. Considering this, another possible interpretation is to merge the first two generations in the SW into one. We opted for two separate generations in this work, because they are consecutive generations and therefore this decision does not have an impact on the succeeding network analyses in time steps.

Gen. 2 is more distinct in NE1 than NE2 where gen. 1 is spaced more narrowly, restraining the development of

440   younger fractures on one hand and causing them to appear like gen. 5 on the other hand, possibly leading to a mix-up in the interpretation of the generations.

Generation 3 is present in all domains in the SW but absent in the NE. The fading of such a distinct fracture generation over a relatively short distance of 200 meters can have a mechanical cause but could also be explained by a wrong association of fractures with other generations. The geometry and distribution of preexisting fractures

445   strongly influences the development of younger generations, possibly leading local variations. Considering that generation 1 and 2 in the SW could belong to the same set, gen. 2 as mapped in the NE could be associated with generation 3 in the SW. This would mean that all domains incorporate the same generations but with local variations in their geometry. Based on our analysis with five spatially isolated domains, this is a question that cannot be answered easily, but requires a continuous tracing of the fracture generations over the complete distance.

450   This interpretation does not have an impact on the network evolution analysis, because the generations are merged in the same order, but highlights necessity of a complete automatic tracing and interpretation of the whole outcrop. Generation 4 also referred to as left-stepping arrays as in (Rawnsley et al., 1998) are consistent in their geometry in all 5 subareas, indicating a larger stress field as reason of the fracturing.

Generation 5 fractures, that result in polygonal patterns are generally shorter than the other fracture generations (<

455   0.5 m) and present in all areas. They show maxima in strike in N-S and E-W directions (Figures 11 and 12), which appear to be caused by the influence of preexisting fractures, e.g. in the NE2, where gen. 5 strikes between 20° and 60°, which is orthogonal to gen.1 fractures, representing the shortest connection between those.

For most cases we expect and observe that younger fractures are shorter than older ones when preexisting fractures restrain their development and thus maximum lengths. Counterintuitive to that, our gen.1 fractures can be shorter

460   than gen.2 and gen. 3 fractures shorter than gen. 4 (Tables 3 and 4). We accredit this anomaly in the case of gen. 1 and 2 to the selection and orientation of our domains relative to the gen. 1 fractures as previously explained. The orientation of gen. 3 is subparallel to preexisting generations, thus the fractures are more likely to abut. This is not the case for gen. 4, which is sub-orthogonal to generations 1 and 2 und thus more likely to protrude through existing fractures, because the underlying stress cannot be accommodated sufficiently by the existing fractures. Another

465   possible explanation is a stronger cementation of gen. 1 and 2 fractures between the events causing gen. 3 and 4, that allows younger fractures to crosscut older, recemented ones.

The sinuosity of all fractures is low on average indicating that they are rather straight than curved over lengths covered in our detailed areas. Higher sinuosity can be expected e.g., for the radially converging (gen.1 NE)

fractures when measured over the complete fracture length and not over a length defined by the dimensions of our

470   mapping domains. We infer that larger mapping areas will lead to better results but also more intensive mapping times. Fracture geometry in the pavement can change over a distance of tens of meters (e.g. between NE1 and NE2 or the domains in the SW and NE), while the geometry and distribution of older fracture sets can strongly influence the geometry and appearance of younger ones.

5.3 Network analysis

475   Analyzing the distribution and geometry of the branches shows that both can change over distances of a few meters within the same limestone layer. These changes may follow a local trend, e.g. decreasing skewness of the distribution from W to E, but can also fluctuate strongly, e.g. in the number of branches and thus the resulting P_{21} fracture intensity, which has a difference of almost a third from the highest value in SW2 to the lowest in NE2. Node distributions are linked to the number of branches and the way they interact. The decrease of I nodes from

480   SW to NE suggests a local trend; however, this assumption is not backed by the numbers of Y nodes, which fluctuate over short distances, e.g. from 2517 to 5100 from NE2 to NE1, a percentage difference of 68%. This underlines the heterogeneity of the fracture network, even though it might appear relatively homogeneous when observed qualitatively, and the necessity in sampling representative domains, when it is not possible to map the complete fracture network.

485   Topological analyses of the fracture network evolution show that average branch lengths decrease with additional fracture generations. This is expected for non-parallel fracture sets which will eventually abut or crosscut each other, contemporaneously increasing the count of Y or X nodes. We identified nodes with more than four branches intersecting at one point in both, manually and automatically extracted traces. Depending on the number of intersecting branches, these nodes are treated as special cases of X nodes: Penta- (5), Hexa- (6), Hepta- (7) or Octa-

490   (8) nodes. Due to the widespread erosion of the fractures at the surface, it is not possible to tell macroscopically, whether these are narrowly spaced X and/or Y nodes or true nodes of a higher degree. In a spatially dense and strongly connected fracture network, we consider it as possible.

Isolated (I) nodes are more numerous in the initial network stages, where fractures have more space to develop and propagate through the limestone without encountering stress shadows of pre-existing fractures. At later stages,

495   most of the I nodes have been connected to other fractures reducing their overall number. Compared to Y or X nodes, the number of I nodes is much lower in general, except for the initial fracture generations. In some cases, initial I nodes of old fracture generations appear to abut to younger fractures. Reasons might be the reactivation of the fracture, or younger fractures connecting with the tip of the pre-existing ones. In cases like this, a unique interpretation is not always possible because abutting criteria become unreliable and other criteria such as length

500   and strike must be considered to aid the interpretation.

The number of Y nodes increases when generations of similar orientation interact with each other or short undirected fractures connect larger ones. X nodes are often the result of intersecting fractures with orthogonal or sub-orthogonal orientation. Nodes of higher degree (5+ branches) are the result of X nodes, to which a younger fracture (mostly gen. 5) abuts. This is possibly caused by the local stress field, in which the existing node represents

505   a zone of weakness to which later developing fractures converge.

As expected for a network with an increasing number of nodes due to an increasing number of non-parallel fractures, branch lengths decrease with more crosscutting/abutting fractures. The longer the crosscutting fracture

and the larger the deviation from the other fracture sets strike, the larger the decrease of the average branch length of the network (longer fractures can potentially cut more fractures).

510 Tables 5-9 show the development of branch lengths within the same order of magnitude over all subareas studied. Especially in the final or recent stage of the network, the average branch lengths are very similar. This indicates that the last fracture generation has a strong impact on the overall network topology. Older fracture generations have a larger influence on network geometry, because pre-existing fractures influence the geometry of the upcoming fracture generations in terms of possible fracture lengths and distribution. However, the topology can 515 be very similar when younger fracture generations overprint the network.

6 Conclusions

- The five inferred fracture generations are not equally distributed throughout our five selected areas; the spatial variation can be significant in the same layer.
520 - The connectivity of the fracture network increased over time while different generations have a different impact on the overall connectivity based on their fracture numbers and orientation to pre-existing fractures.
- Later fracture generations are influenced by preceding fracture generations.
- The network topology and connectivity in this area is strongly influenced by the last generation.
- Nodes with more than four intersecting branches are possible in this fracture network.
525 - When mapping within a 2D boundary, the selected size of the mapping area can impact the measurements, e.g. when the largest fractures are longer than the outlines of the mapping boundary.
- While manual mapping is superior to the automatic mapping procedure, the required time can be reduced, and results of comparable quality produced.
- The automatic interpretation of fracture generations is not yet possible and requires manual input.

530

Code availability. The code used for automatic fracture tracing is published in Prabhakaran, R., Bruna, P.-O., Bertotti, G. and Smeulders, D.: An automated fracture trace detection technique using the complex shearlet transform, Solid Earth, 10(6), 2137–2166, doi:10.5194/se-10-2137-2019, 2019. The code is available on Github https://github.com/rahulprabhakaran/Automatic-Fracture-Detection-Code/tree/v1.0.0 (last access: 30 535 March 2020; see https://doi.org/10.5281/zenodo.3245452).

Data availability. Shapefiles of the fracture traces presented in this manuscript are provided in the supplement.

Author contribution. All authors contributed to the discussion and commented on the manuscript. CW acquired, 540 processed and evaluated the data and has written the manuscript with input of the co-authors. RP contributed the automatically traced fractures and helped with the preparation of the manuscript. MP contributed to the manual mapping of fractures and the initial interpretation of fracture generations. JLU gave the impulse to this work, provided the funding and contributed to the conceptualization. GB contributed to the discussion and structure of the manuscript. KR contributed to the conceptualization and provided input during the manuscript preparation.

545

Competing interests. The authors declare that they have no conflict of interest.

References

Andrews, B. J., Roberts, J. J., Shipton, Z. K., Bigi, S., Tartarello, M. C. and Johnson, G.: How do we see fractures?

550   Quantifying subjective bias in fracture data collection, Solid Earth, 10(2), 487–516, doi:10.5194/se-10-487-2019, 2019.

Agheshlui, H., Sedaghat, M. H. and Matthai, S.: Stress Influence on Fracture Aperture and Permeability of Fragmented Rocks, J. Geophys. Res. Solid Earth, 123(5), 3578–3592, doi:10.1029/2017JB015365, 2018.

555

Agisoft,   (2017).   PhotoScan   Professional   (Version   1.3.2)   [Software].   Retrieved   from https://www.agisoft.com/downloads/installer/

Azizmohammadi, S. and Matthäi, S. K.: Is the permeability of naturally fractured rocks scale dependent?, Water

560   Resour. Res., 53(9), 8041–8063, doi:10.1002/2016WR019764, 2017.

Belayneh, M. and Cosgrove, J. W.: Fracture-pattern variations around a major fold and their implications regarding fracture prediction using limited data: an example from the Bristol Channel Basin, Geol. Soc. Lond. Spec. Publ., 231(1), 89–102, doi:10.1144/GSL.SP.2004.231.01.06, 2004.

565

Belayneh, M., Geiger, S. and Matthäi, S. K.: Numerical simulation of water injection into layered fractured carbonate reservoir analogs, AAPG Bull., 90(10), 1473–1493, doi:10.1306/05090605153, 2006a.

Belayneh, M., Masihi, M., Matthäi, S. K. and King, P. R.: Prediction of vein connectivity using the percolation

570   approach: model test with field data, J. Geophys. Eng., 3(3), 219–229, doi:10.1088/1742-2132/3/3/003, 2006b.

Bemis, S. P., Micklethwaite, S., Turner, D., James, M. R., Akciz, S., Thiele, S. T. and Bangash, H. A.: Ground-based and UAV-Based photogrammetry: A multi-scale, high-resolution mapping tool for structural geology and paleoseismology, J. Struct. Geol., 69, 163–178, doi:10.1016/j.jsg.2014.10.007, 2014.

575

Bevan, T. G. and Hancock, P. L.: A late Cenozoic regional mesofracture system in southern England and northern France, J. Geol. Soc., 143(2), 355–362, doi:10.1144/gsjgs.143.2.0355, 1986.

Bisdom, K., Nick, H. M. and Bertotti, G.: An integrated workflow for stress and flow modelling using outcrop-

580   derived discrete fracture networks, Comput. Geosci., 103, 21–35, doi:10.1016/j.cageo.2017.02.019, 2017.

Brooks, M., Trayner, P. M. and Trimble, T. J.: Mesozoic reactivation of Variscan thrusting in the Bristol Channel area, UK, J. Geol. Soc., 145(3), 439–444, doi:10.1144/gsjgs.145.3.0439, 1988.

585   Crider, J. G. and Peacock, D. C. P.: Initiation of brittle faults in the upper crust: a review of field observations, J. Struct. Geol., 26(4), 691–707, doi: 10.1016/j.jsg.2003.07.007, 2004.

Solid Earth
Discussions

Dart, C. J., McClay, K. and Hollings, P. N.: 3D analysis of inverted extensional fault systems, southern Bristol Channel basin, UK, Geol. Soc. Lond. Spec. Publ., 88(1), 393–413, doi:10.1144/GSL.SP.1995.088.01.21, 1995.

590

Dershowitz, W. S. and Herda, H. H.: Interpretation of fracture spacing and intensity, in ARMA-92-0757, p. 10, American Rock Mechanics Association, Santa Fe, New Mexico. [online] Available from: https://doi.org/, 1992.

Dimmen, V., Rotevatn, A., Peacock, D. C. P., Nixon, C. W. and Nærland, K.: Quantifying structural controls on

595   fluid flow: Insights from carbonate-hosted fault damage zones on the Maltese Islands, J. Struct. Geol., 101, 43–57, doi:10.1016/j.jsg.2017.05.012, 2017.

Duelis Viana, C., Endlein, A., Ademar da Cruz Campanha, G. and Henrique Grohmann, C.: Algorithms for extraction of structural attitudes from 3D outcrop models, Comput. Geosci., 90, 112–122,

600   doi:10.1016/j.cageo.2016.02.017, 2016.

Engelder, T. and Peacock, D. C. P.: Joint development normal to regional compression during flexural-flow folding: the Lilstock buttress anticline, Somerset, England, J. Struct. Geol., 23(2), 259–277, doi: 10.1016/S0191-8141(00)00095-X, 2001.

605

Esri (2019). ArcGIS (Version 10.7.1) [Software].

Gillespie, P., Monsen, E., Maerten, L., Hunt, D., Thurmond, J. and Tuck, D., Eds.: Fractures in Carbonates: From Digital Outcrops to Mechanical Models, in Outcrops Revitalized: Tools, Techniques and Applications, SEPM

610   (Society for Sedimentary Geology)., 2011.

Glen, R. A., Hancock, P. L. and Whittaker, A.: Basin inversion by distributed deformation: the southern margin of the Bristol Channel Basin, England, J. Struct. Geol., 27(12), 2113–2134, doi:10.1016/j.jsg.2005.08.006, 2005.

615   Hancock, P. L.: Jointing in the Jurassic limestones of the Cotswold Hills, Proc. Geol. Assoc., 80(2), 219–241, doi:10.1016/S0016-7878(69)80043-X, 1969.

Hancock, P. L. and Engelder, T.: Neotectonic joints, GSA Bull., 101(10), 1197–1208, doi:10.1130/0016-7606(1989)101<1197:NJ>2.3.CO;2, 1989.

620

Hansman, R. J. and Ring, U.: Workflow: From photo-based 3-D reconstruction of remotely piloted aircraft images to a 3-D geological model, Geosphere, 15(4), 1393–1408, doi:10.1130/GES02031.1, 2019.

Kelly, P. G., Peacock, D. C. P., Sanderson, D. J. and McGurk, A. C.: Selective reverse-reactivation of normal

625   faults, and deformation around reverse-reactivated faults in the Mesozoic of the Somerset coast, J. Struct. Geol., 21(5), 493–509, doi:10.1016/S0191-8141(99)00041-3, 1999.

Loosveld, R. J. H. and Franssen, R. C. M. W.: Extensional vs. Shear Fractures: Implications for Reservoir Characterisation, in SPE-25017-MS, p. 8, Society of Petroleum Engineers, Cannes, France., 1992.

630

Matthäi, S. K. and Belayneh, M.: Fluid flow partitioning between fractures and a permeable rock matrix, Geophys. Res. Lett., 31(7), L07602, doi:10.1029/2003GL019027, 2004.

Matthäi, S. K., Mezentsev, A. A. and Belayneh, M.: Finite Element - Node-Centered Finite-Volume Two-Phase-
635   Flow Experiments With Fractured Rock Represented by Unstructured Hybrid-Element Meshes, SPE Reserv. Eval. Eng., 10(06), 740–756, doi:10.2118/93341-PA, 2007.

Mauldon, M., Dunne, W. M. and Rohrbaugh, M. B.: Circular scanlines and circular windows: new tools for characterizing the geometry of fracture traces, J. Struct. Geol., 23(2–3), 247–258, doi:10.1016/S0191-
640   8141(00)00094-8, 2001.

Morley, C. K. and Nixon, C. W.: Topological characteristics of simple and complex normal fault networks, J. Struct. Geol., 84, 68–84, doi:10.1016/j.jsg.2016.01.005, 2016.

645   Müller, D., Walter, T. R., Schöpa, A., Witt, T., Steinke, B., Gudmundsson, M.T. and Dürig, T.: High-Resolution Digital Elevation modeling from TLS and UAV Campaign Reveals Structural Complexity at the 2014/2015 Holuhraun Eruption Site, Iceland, Front Earth Sci, 5, doi:10.3389/feart.2017.00059, 2017.

Nemčok, M., Gayer, R. and Miliorizos, M.: Structural analysis of the inverted Bristol Channel Basin: implications
650   for the geometry and timing of fracture porosity, Geol. Soc. Lond. Spec. Publ., 88(1), 355–392, doi:10.1144/GSL.SP.1995.088.01.20, 1995.

Niethammer, U., James, M. R., Rothmund, S., Travelletti, J. and Joswig, M.: UAV-based remote sensing of the Super-Sauze landslide: Evaluation and results, Eng. Geol., 128, 2–11, doi: 10.1016/j.enggeo.2011.03.012, 2012.

655
Nyberg, B., Nixon, C. W. and Sanderson, D. J.: NetworkGT: A GIS tool for geometric and topological analysis of two-dimensional fracture networks, Geosphere, 14(4), 1618–1634, doi:10.1130/GES01595.1, 2018.

Pahl, P. J.: Estimating the Mean Length of Discontinuity Traces, Int. J. Rock Mech. Min. Sci., 18, 221–228,
660   doi:0148-9062/81/030221-08502.00/0, 1981.

Peacock, D. C. P. and Sanderson, D. J.: Displacements, segment linkage and relay ramps in normal fault zones, J. Struct. Geol., 13(6), 721–733, doi:10.1016/0191-8141(91)90033-F, 1991.

665   Peacock, D. C. P. and Sanderson, D. J.: Geometry and Development of Relay Ramps in Normal Fault Systems, AAPG Bull., 78(2), 147–165, 1994.

Peacock, D. C. P. and Sanderson, D. J.: Strike-slip relay ramps, J. Struct. Geol., 17(10), 1351–1360, doi:10.1016/0191-8141(95)97303-W, 1995.

670

Peacock, D. C. P., Sanderson, D. J. and Rotevatn, A.: Relationships between fractures, J. Struct. Geol., 106, 41–53, doi:10.1016/j.jsg.2017.11.010, 2018.

Peacock, D. C. P., Sanderson, D. J., Bastesen, E., Rotevatn, A. and Storstein, T. H.: Causes of bias and uncertainty
675   in fracture network analysis, NJG, 99(1), 113–128, doi:10.17850/njg99-1-06, 2019.

Pix4D SA (Pix4D AG) (Pix4D Ltd), (2017). Pix4Dcapture (Version 2.1.0) [iOS application]. Retrieved from https://apps.apple.com/de/app/pix4dcapture/id953486050

680   Prabhakaran, R., Bruna, P.-O., Bertotti, G. and Smeulders, D.: An automated fracture trace detection technique using the complex shearlet transform, Solid Earth, 10(6), 2137–2166, doi:10.5194/se-10-2137-2019, 2019.

Priest, S. D. and Hudson, J. A.: Estimation of Discontinuity Spacing and Trace Length Using Scanline Surveys, Int. J. Rock Mech. Min. Sci., 18, 183–197, doi:0148-9062/81/030183-15502.00/0, 1981.

685

Procter, A. and Sanderson, D. J.: Spatial and layer-controlled variability in fracture networks, J. Struct. Geol., 108, 52–65, doi:10.1016/j.jsg.2017.07.008, 2018.

Rawnsley, K. D., Peacock, D. C. P., Rives, T. and Petit, J.-P.: Joints in the Mesozoic sediments around the Bristol
690   Channel Basin, J. Struct. Geol., 20(12), 1641–1661, doi:10.1016/S0191-8141(98)00070-4, 1998.

Reisenhofer, R., Kiefer, J. and King, E. J.: Shearlet-based detection of flame fronts, Exp. Fluids, 57(3), doi:10.1007/s00348-016-2128-6, 2016.

695   Rohrbaugh, M. B., Dunne, W. M. and Mauldon, M.: Estimating fracture trace intensity, density, and mean length using circular scan lines and windows, AAPG Bull., 86, doi:10.1306/61EEDE0E-173E-11D7-8645000102C1865D, 2002.

Sanderson, D. J. and Nixon, C. W.: The use of topology in fracture network characterization, J. Struct. Geol., 72,
700   55–66, doi:10.1016/j.jsg.2015.01.005, 2015.

Vasuki, Y., Holden, E.-J., Kovesi, P. and Micklethwaite, S.: Semi-automatic mapping of geological Structures using UAV-based photogrammetric data: An image analysis approach, 25.04.2014, 69, 22–32, 2014.

705   Watkins, H., Bond, C. E., Healy, D. and Butler, R. W. H.: Appraisal of fracture sampling methods and a new workflow to characterise heterogeneous fracture networks at outcrop, J. Struct. Geol., 72, 67–82, doi:10.1016/j.jsg.2015.02.001, 2015.

Weismüller, C., Urai, J. L., Kettermann, M., von Hagke, C. and Reicherter, K.: Structure of massively dilatant
710   faults in Iceland: lessons learned from high-resolution unmanned aerial vehicle data, Solid Earth, 10(5), 1757–
1784, doi:10.5194/se-10-1757-2019, 2019.

Westoby, M. J., Brasington, J., Glasser, N. F., Hambrey, M. J. and Reynolds, J. M.: 'Structure-from-Motion'
photogrammetry: A low-cost, effective tool for geoscience applications, Geomorphology, 179, 300–314, doi:
715   10.1016/j.geomorph.2012.08.021, 2012.

Wu, H. and D. Pollard, D.: An experimental study of the relationship between joint spacing and layer thickness, J.
Struct. Geol., 17(6), 887–905, doi:10.1016/0191-8141(94)00099-L, 1995.

720
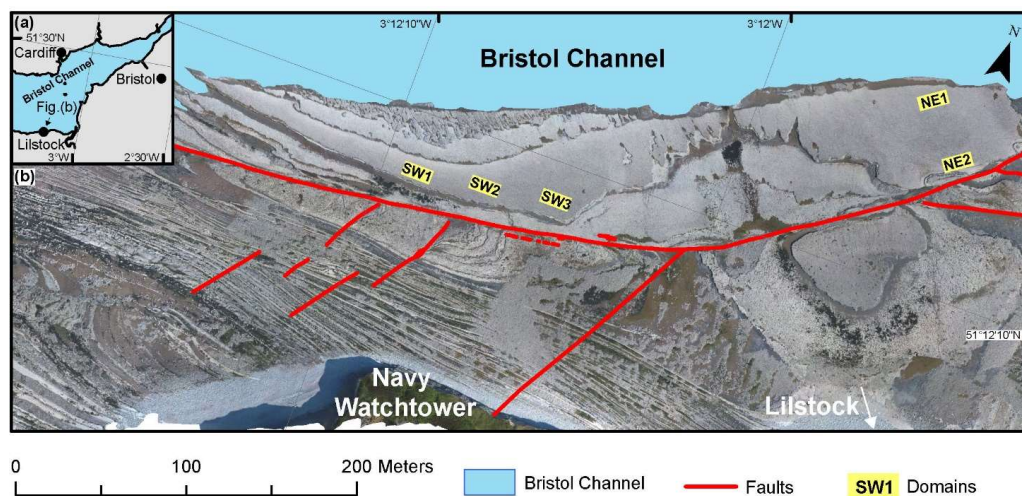
Fig. 1: (a) Location of the study area in the Bristol Channel, Great Britain. (b Ortho-rectified photo-mosaic of UAV-photographs taken from 100 m. The ortho-mosaic shows the coast at Lilstock during low tide, exposing the fractured limestone. The study areas on "the bench" that are mapped in detail are marked in
725   **red.**
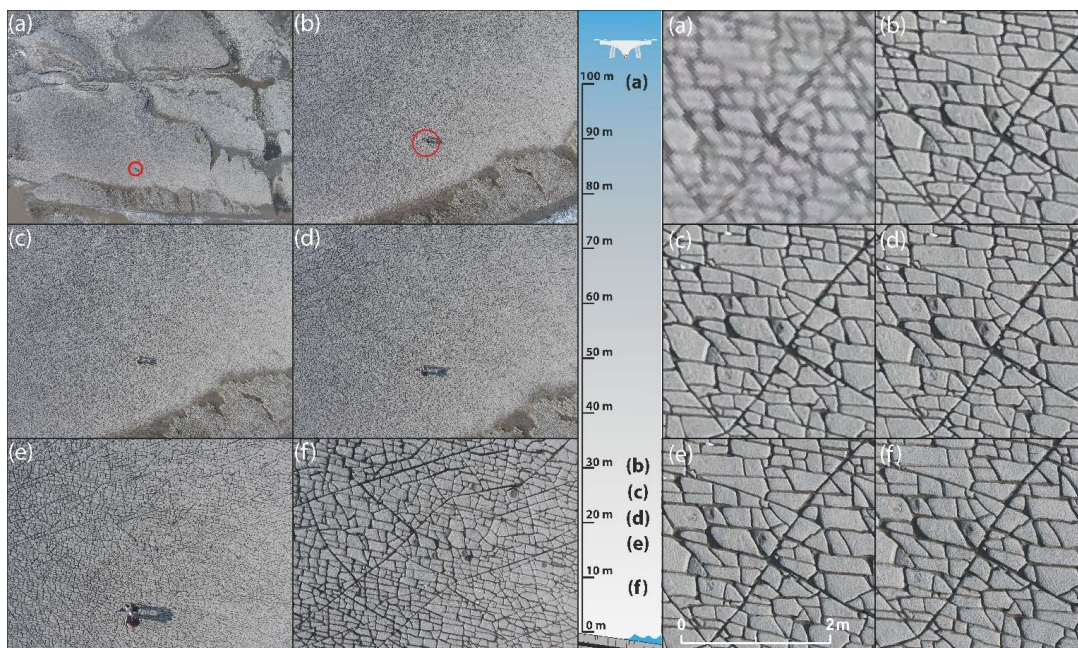
Fig. 2: The fractured limestone captured from above by UAV. Left: View from different altitudes with altitudes decreasing from (a) to (f). The exact altitudes from which the photographs have been taken can be viewed in the sketch in the center. Right: Same photographs as on the left, zoomed in to the same degree in every image. With increasing altitude, the spatial resolution of the image decreases.
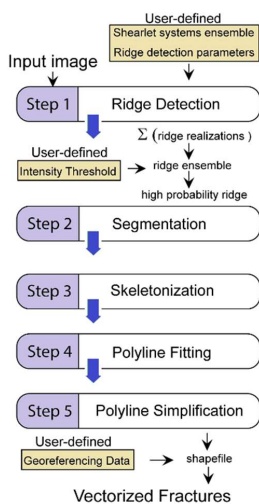
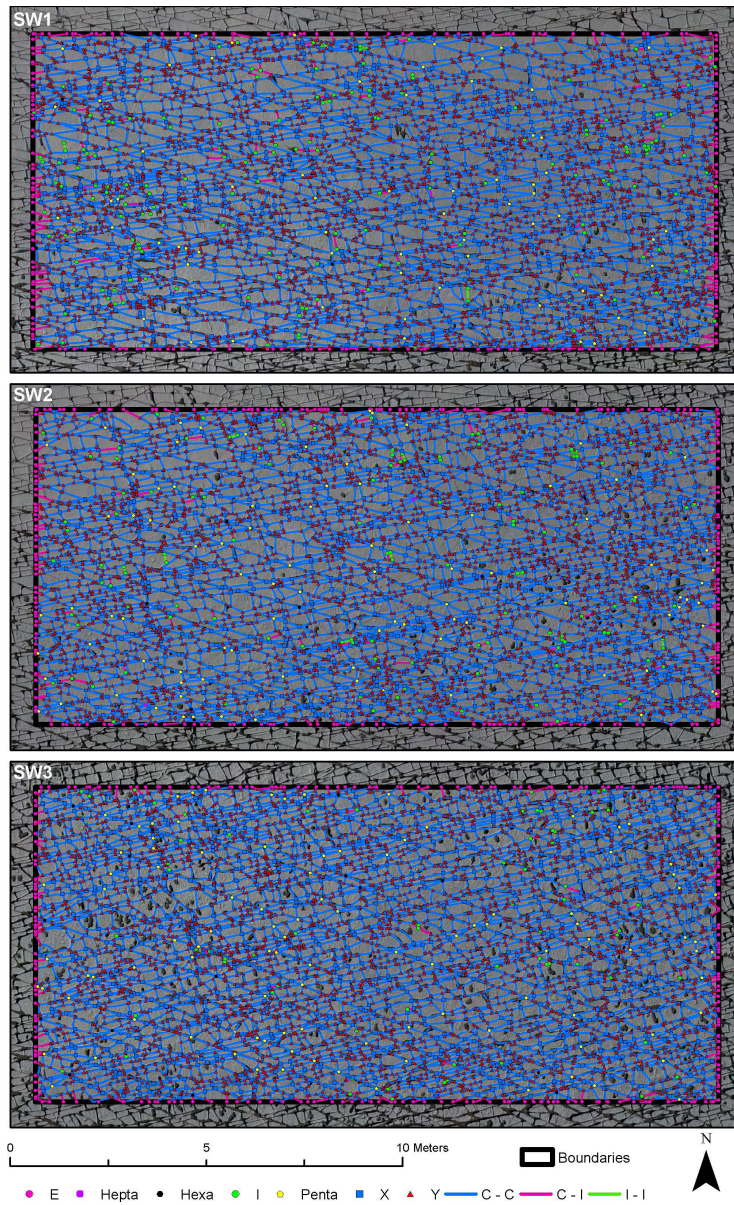**Fig. 3: Overview of the automated fracture detection process (reproduced with permission from Prabhakaran et al, 2019)**
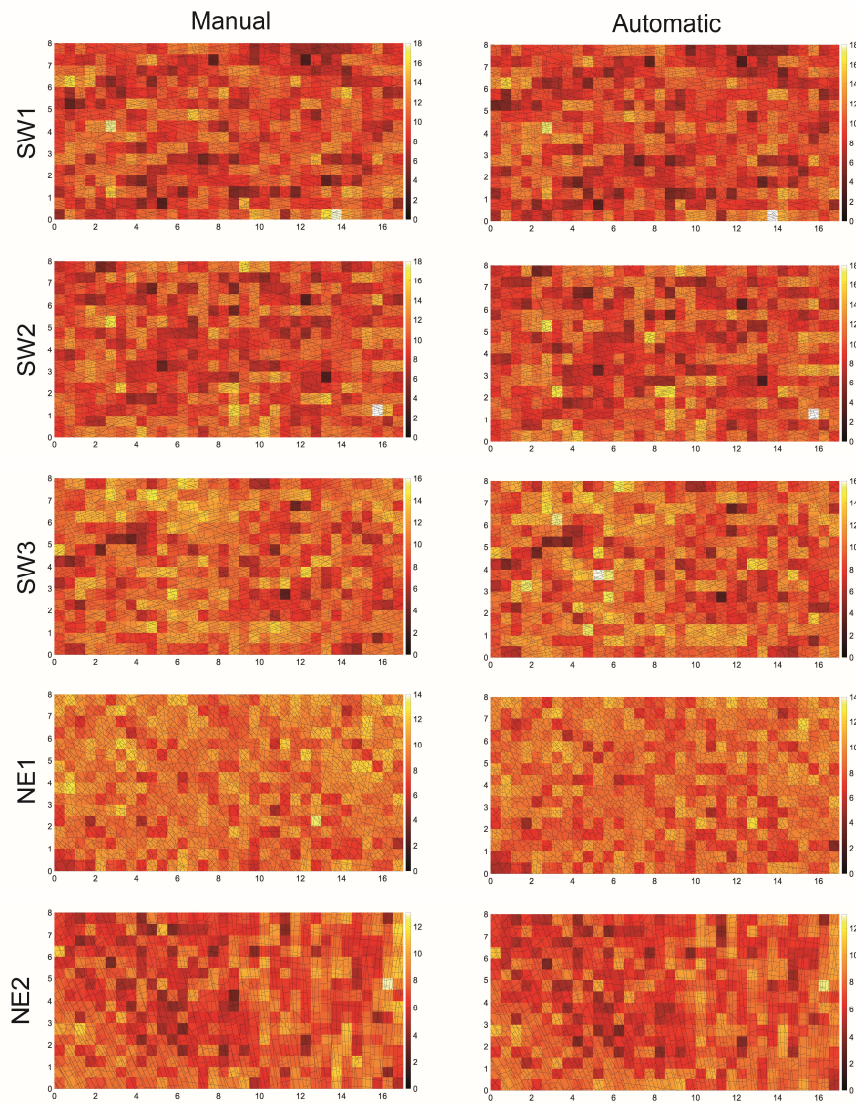
Fig. 4: P$_{21}$ plots of the mapped fractures within the 5 subareas for the manual and automatic interpretations. Unit of the axes in (m), unit of the color bar in (m/m²).

Fig. 5: SW fracture networks, automatically traced and plotted as branches and nodes.
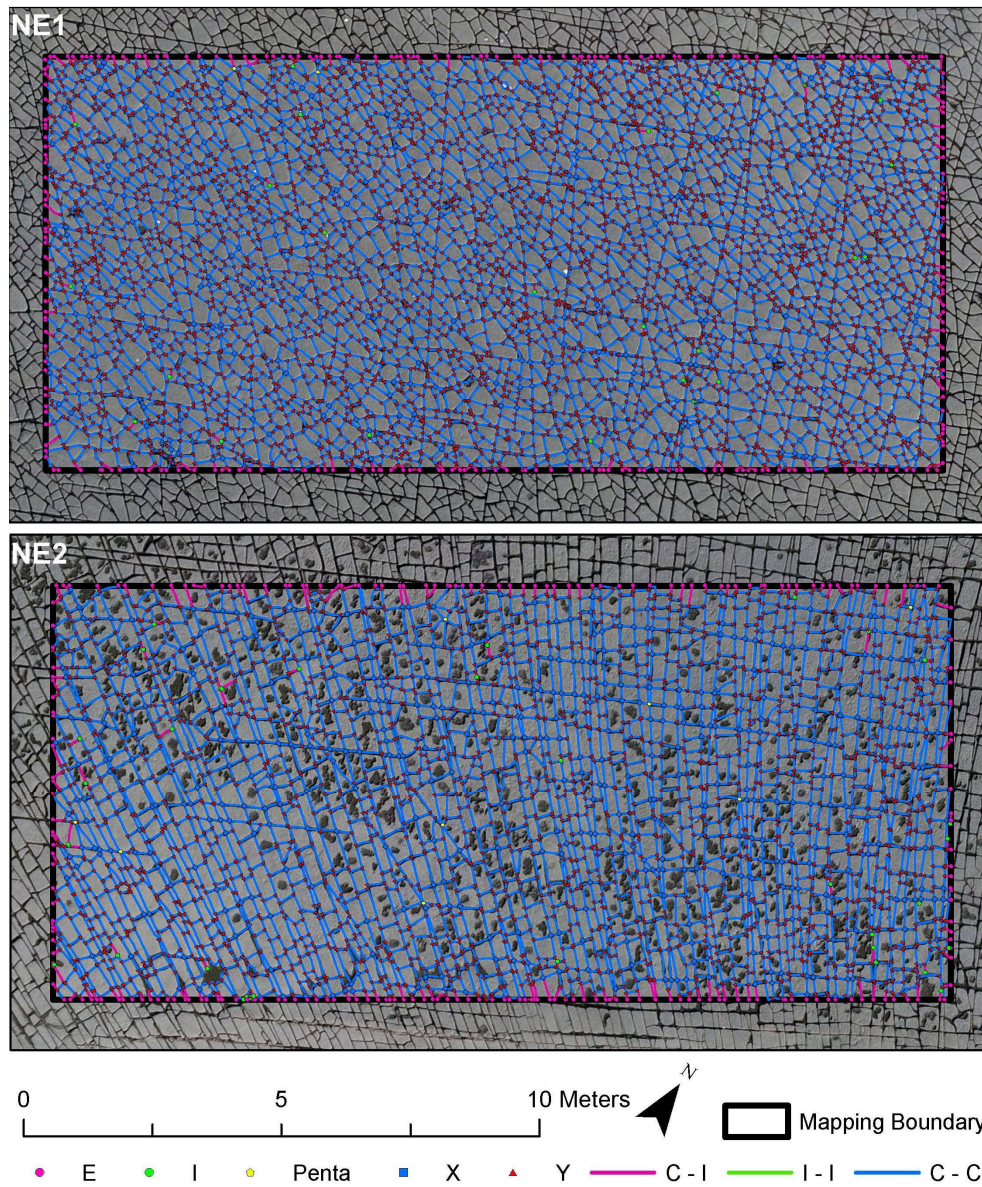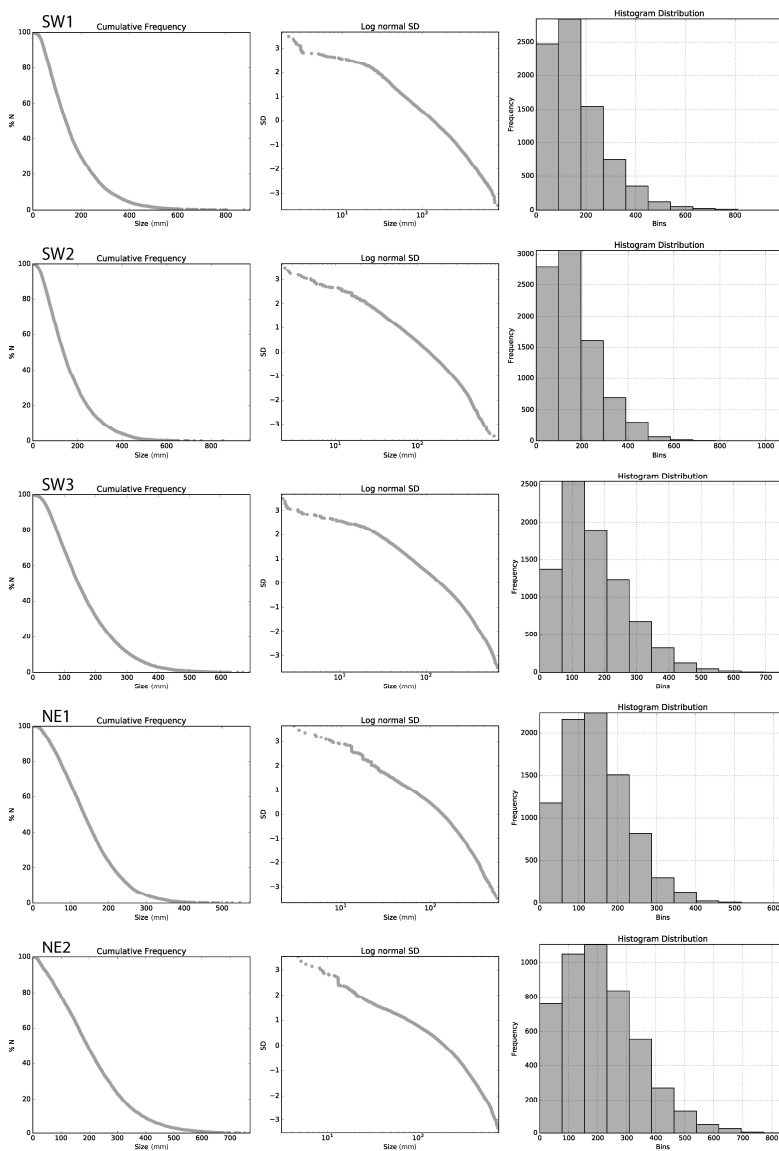
Fig. 6: NE fracture networks, automatically traced and plotted as branches and nodes.

745 **Fig. 7: Cumulative length distribution, log normal standard deviation and histogram distributions of the automatically traced fractures in the five domains.**
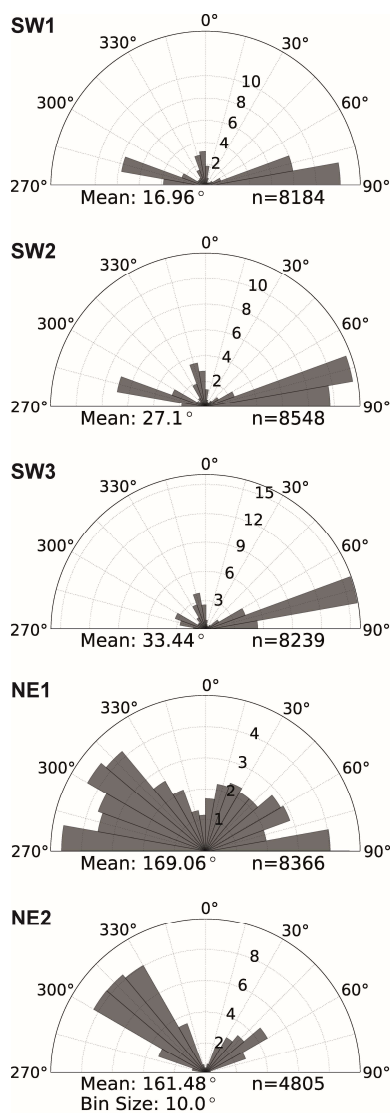
Fig. 8: Length weighted rose plots of automatically traced fractured in the five domains.
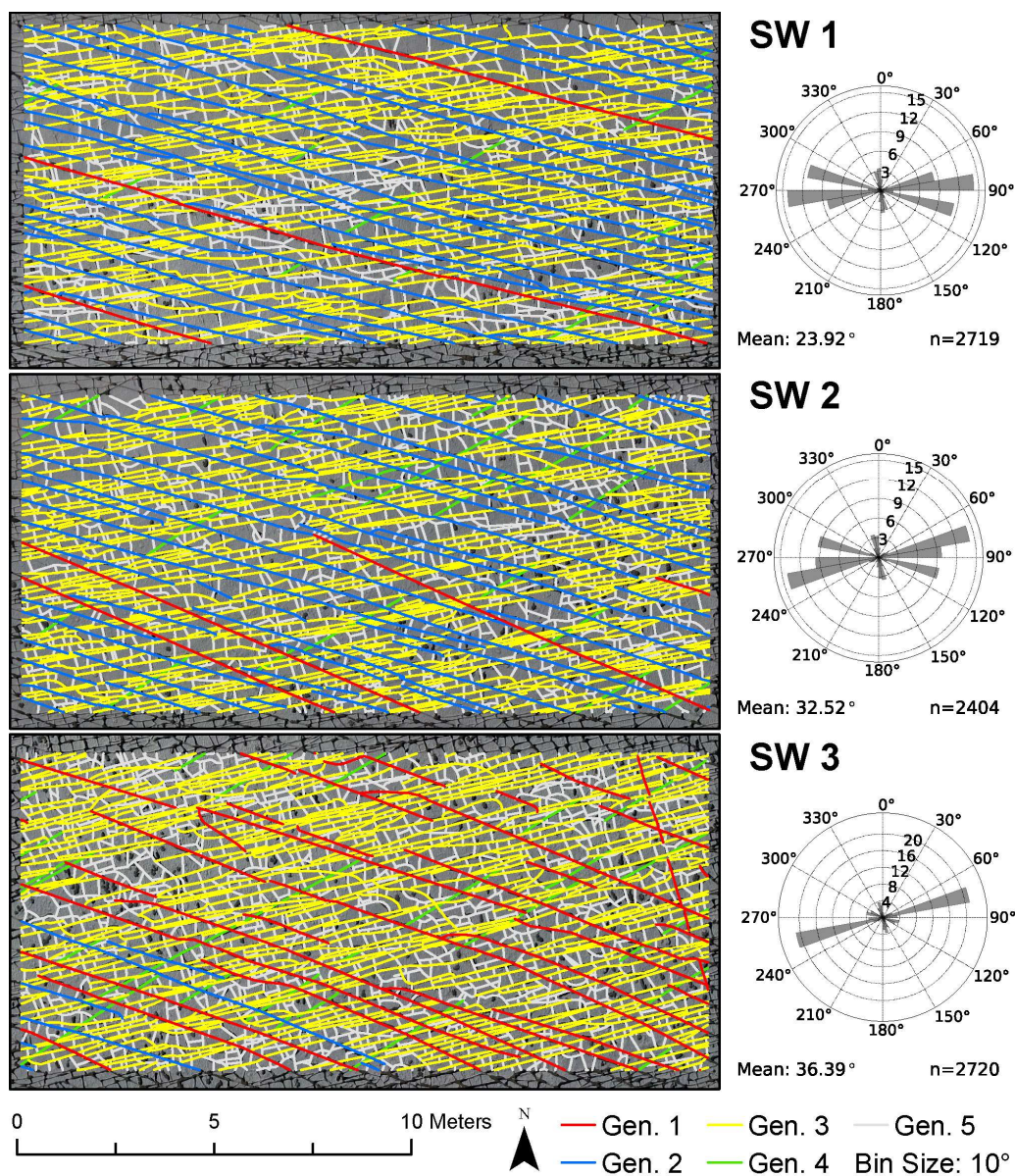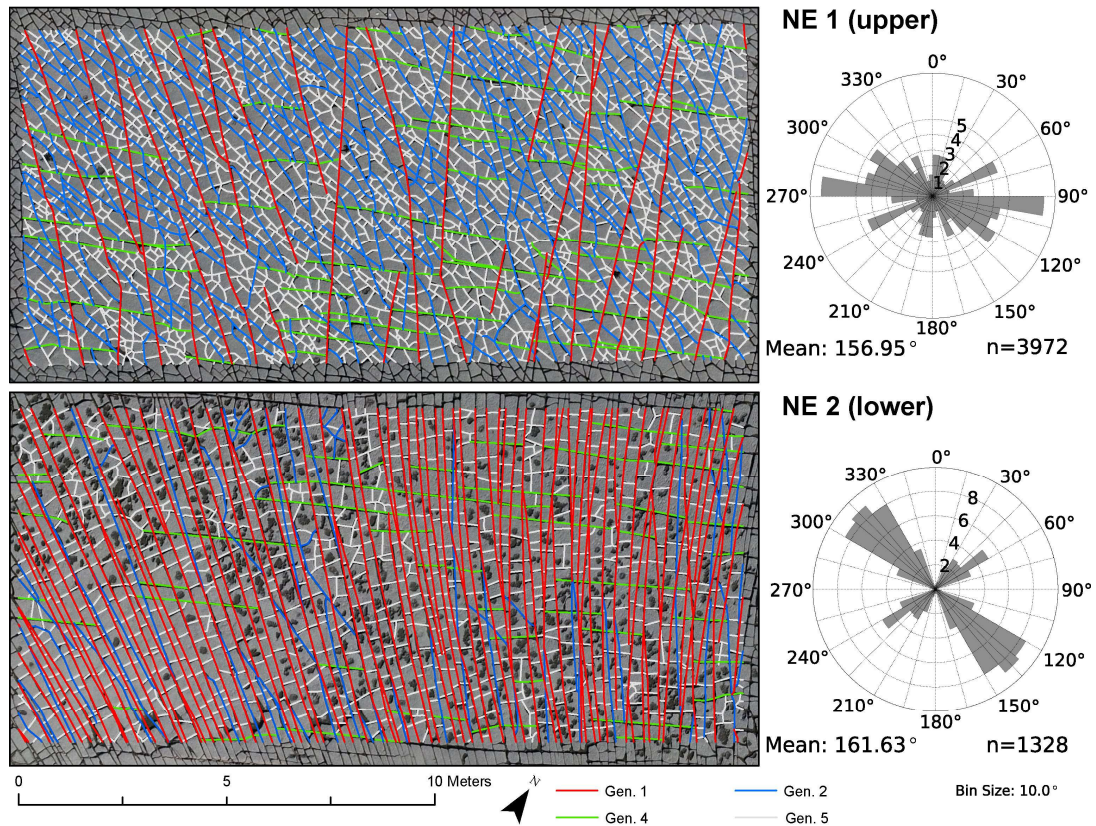
750

Fig. 9: Interpretation of fracture generations in the domains in the SW. Fracture orientations are visualized as length weighted rose plots.

Fig. 10: Interpretation of fracture generations in the domains in the NE. Fracture orientations are visualized as length weighted rose plots. Note that the fracture networks on the left are oriented NW-SE.

Fig. 11: Plots of strike direction (°) on the x-axis and length (m) on the y-axis for every fracture mapped in the domains in the SW, color coded by generation.
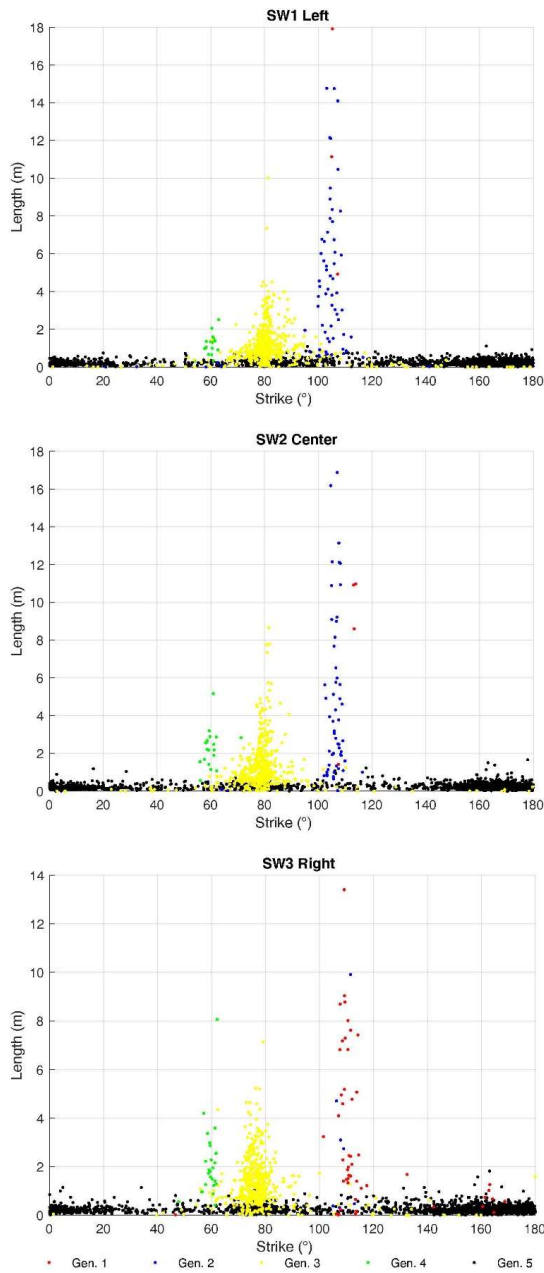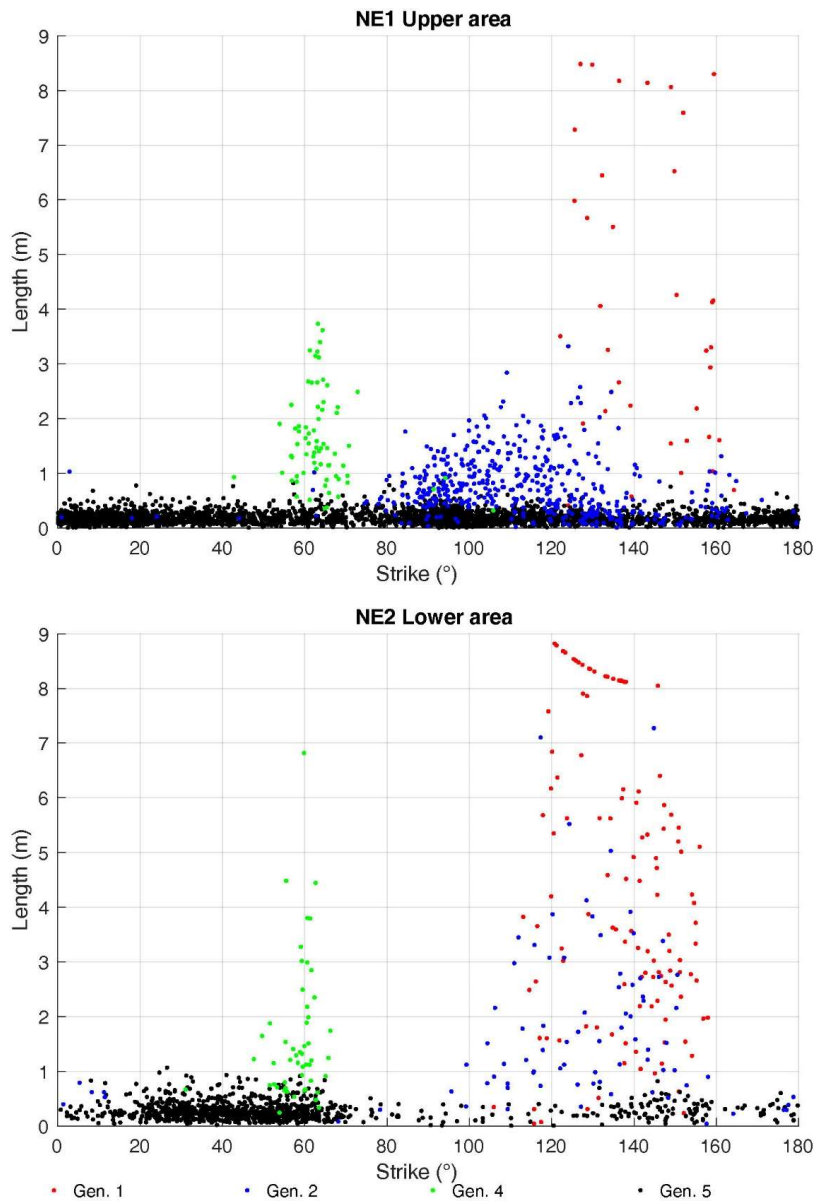
Fig. 12: Plots of strike direction (°) on the x-axis and length (m) on the y-axis for every fracture mapped in the domains in the NE, color coded by generation.

Fig. 13: Development of the fracture network in time steps for SW1, visualized as branches and nodes. The consecutive fracture generation is added for each panel from (a) to (e).

795
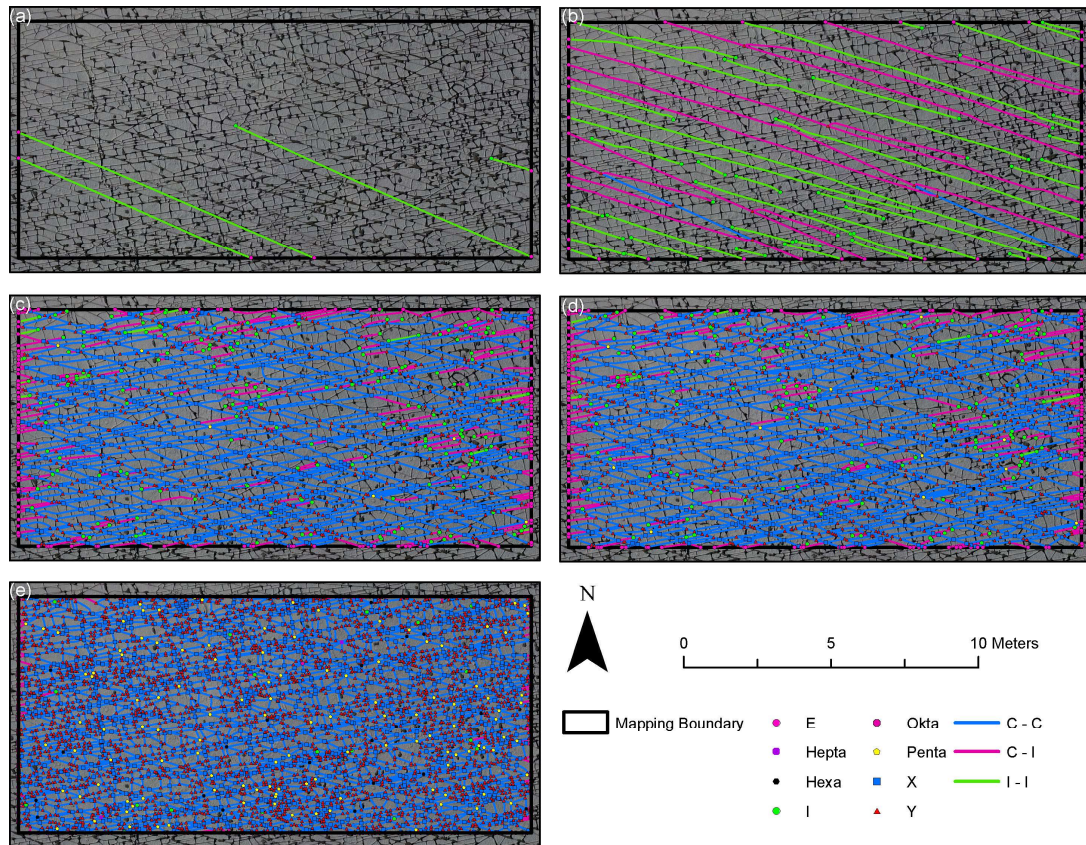
Fig. 14: Development of the fracture network in time steps for SW2, visualized as branches and nodes. The consecutive fracture generation is added for each panel from (a) to (e).

800
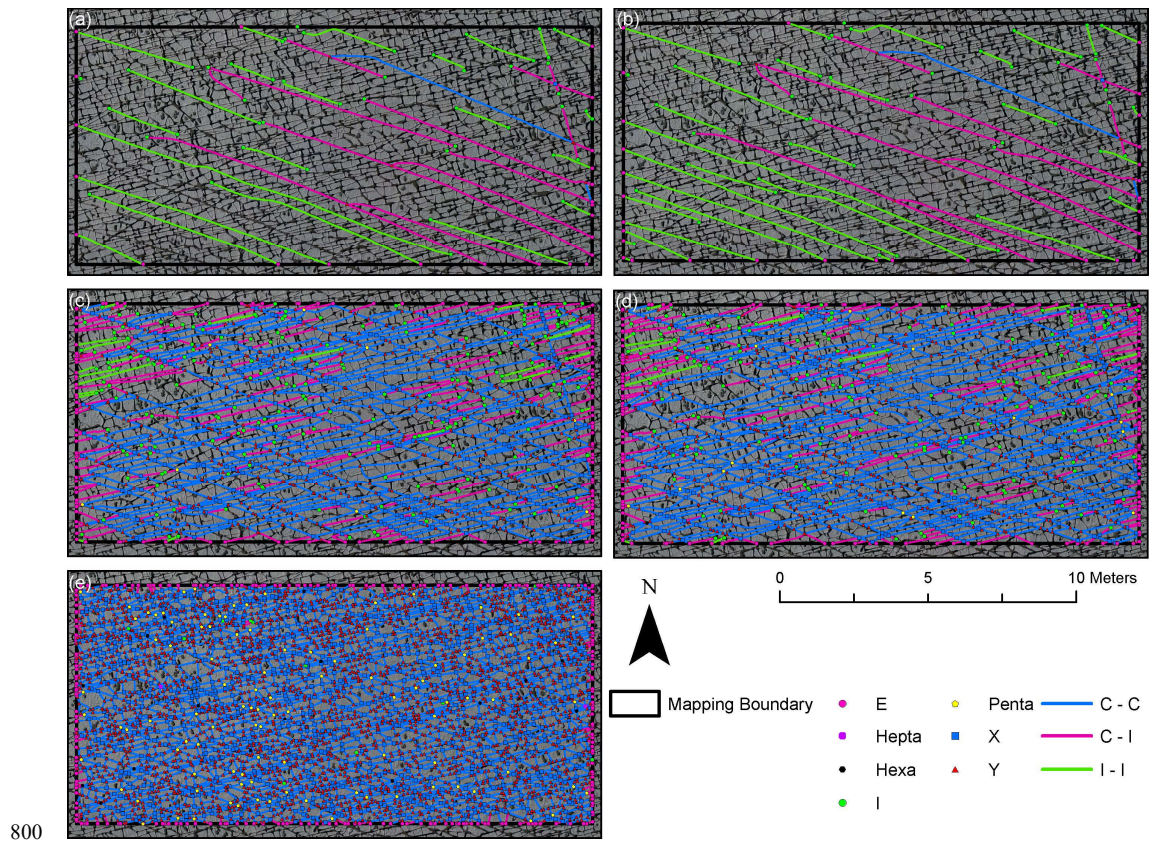
Fig. 15: Development of the fracture network in time steps for SW3, visualized as branches and nodes. The consecutive fracture generation is added for each panel from (a) to (e).

Solid Earth
Discussions
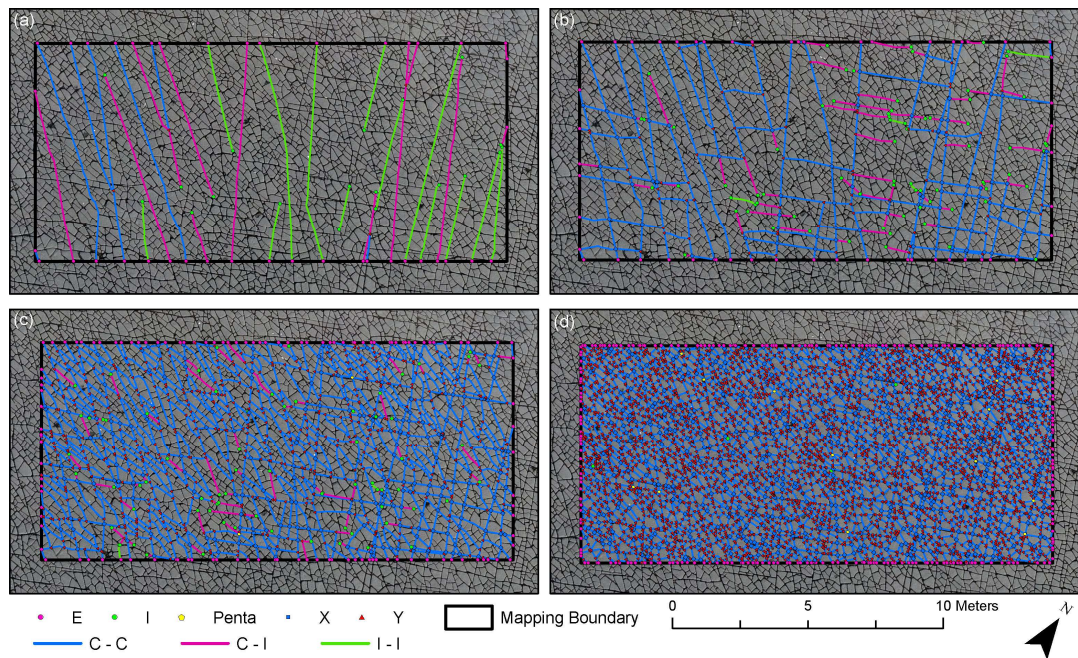
Fig. 16: Development of the fracture network in time steps for NE1, visualized as branches and nodes. The consecutive fracture generation is added for each panel from (a) to (d).
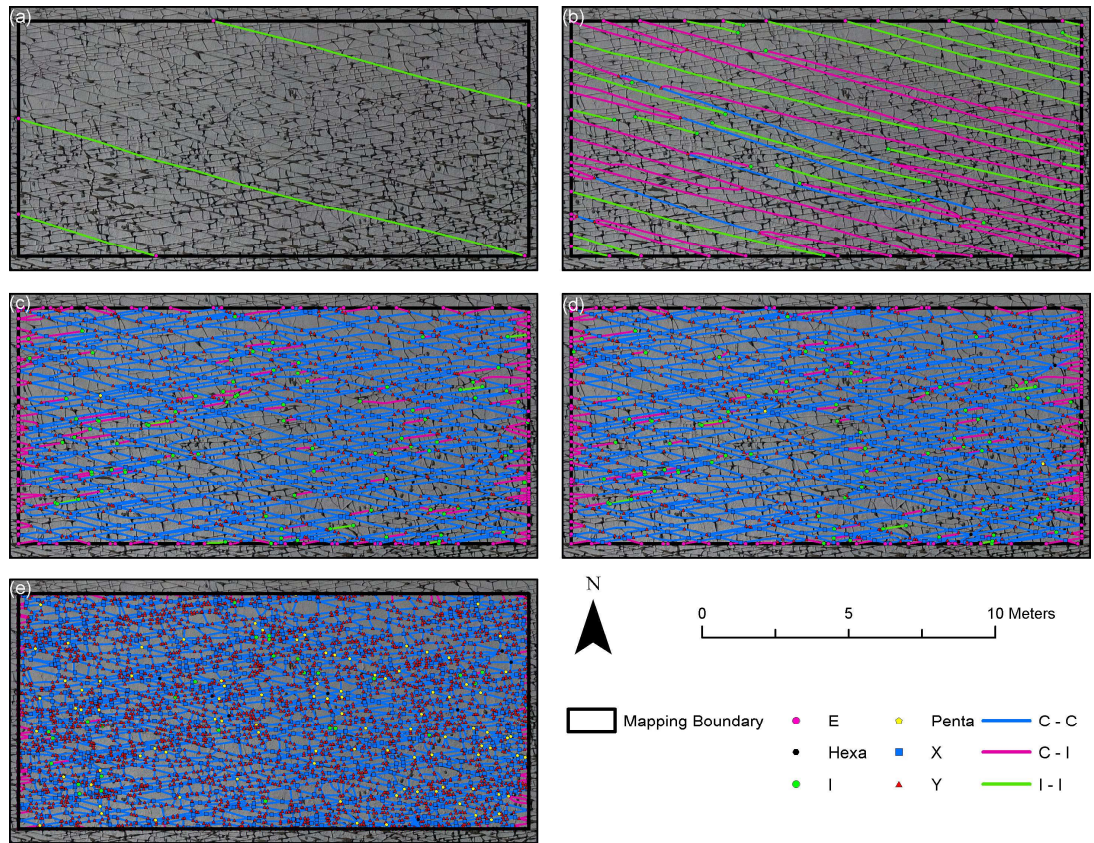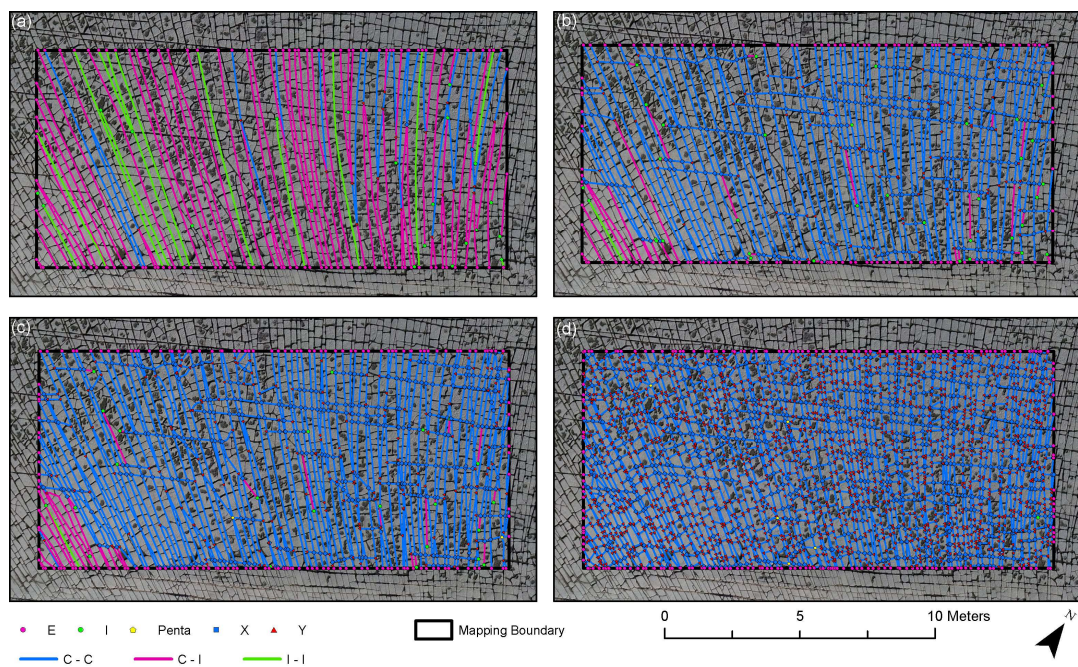

Fig. 17: Development of the fracture network in time steps for NE2, visualized as branches and nodes. The consecutive fracture generation is added for each panel from (a) to (d).
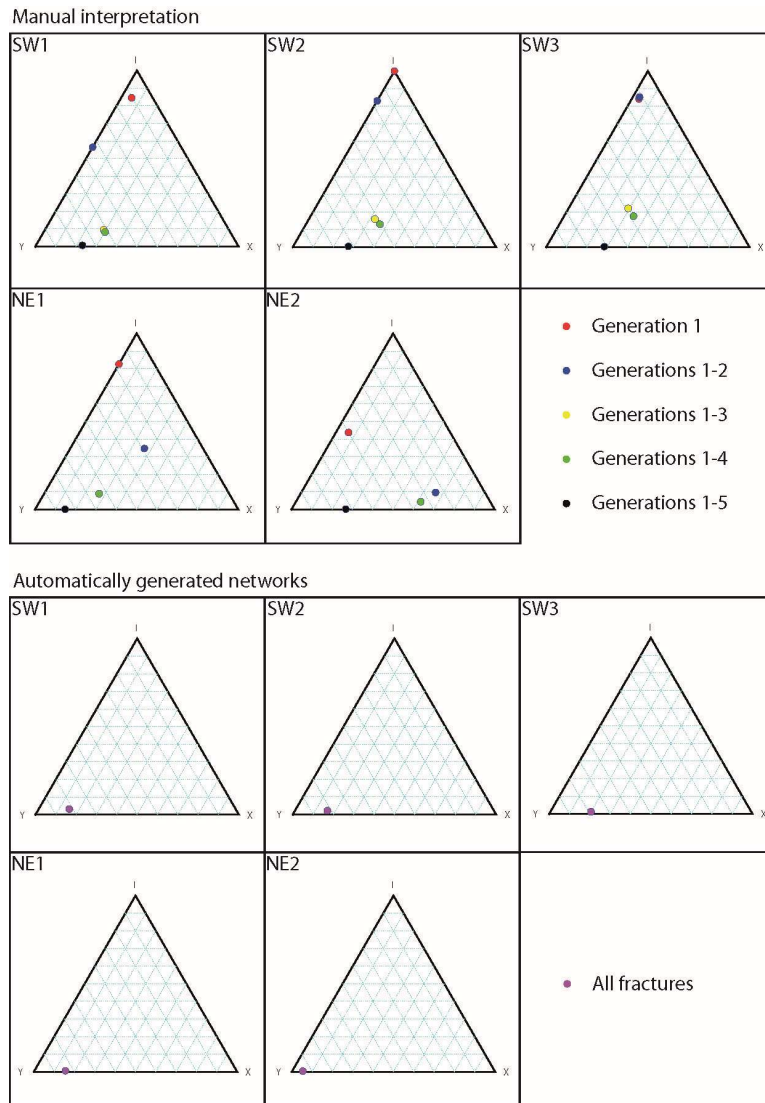
Fig. 18: Ternary plots visualizing the node distributions. For the manual interpretations, the different network stages in terms of fracture generations are plotted. The automatic networks only show the final stage of the network, which corresponds to generations 1 – 5 in the manual interpretation. Nodes with four and more than four intersecting branches have been binned as type X nodes.
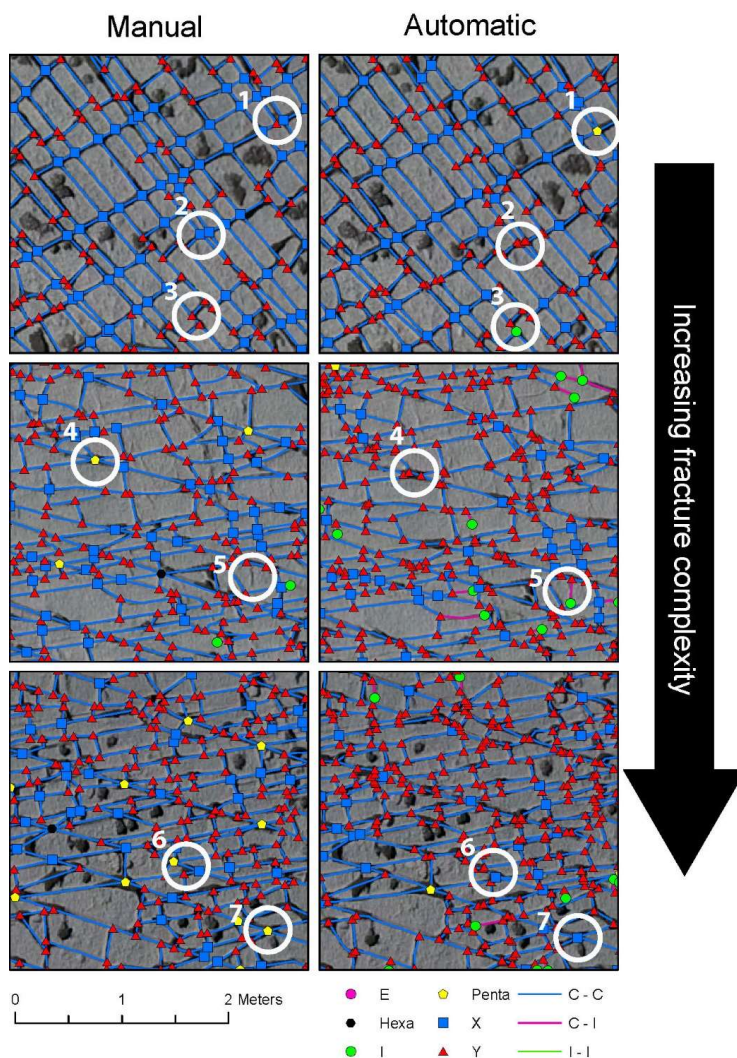
Fig. 19: Comparison of the resulting network analysis from manual (left) and automatic (right) mapping. The complexity of the fracture patterns increases top to bottom; therefore, the quality of the results is assumed to decrease. Marks 1 - 6 show differences of the manual and automatic interpretation. 1) Two closely spaced Y and X nodes (manual) or one Penta node (automatic); 2) X nodes (manual) or closely spaced Y nodes (automatic); 3) Abutting fracture (manual) or I node (automatic); 4) One Penta node (manual) or three Y nodes (automatic); 5) Interpretation as surface erosion or a small fracture; 6) Penta and X nodes (manual) or X and Y nodes (automatic); 7) Interpretation as two close fractures resulting in a Penta node (manual) or as one fracture resulting in a X node.

Table 1: P$_{21}$ analysis and statistics of the fracture networks.

	SW 1	SW 2	SW 3	NE 1	NE 2
Branches	8184	8548	8239	8366	4831
P$_{21}$ (m^{-1})	9.7	10.01	9.84	8.75	7.31
Mean (m)	0.16	0.16	0.17	0.15	0.21
Geom. mean (m)	0.13	0.13	0.13	0.12	0.17
Standard deviation	0.12	0.11	0.1	0.08	0.13
25%	0.08	0.08	0.09	0.08	0.11
50%	0.14	0.14	0.14	0.14	0.19
75%	0.22	0.22	0.23	0.2	0.29
Min.	< 1 cm	< 1 cm	< 1 cm	< 1 cm	< 1 cm
Max.	0.9	0.97	0.69	0.57	0.77
Covariance	0.7	0.67	0.62	0.56	0.62
Skewness	1.46	1.21	1.01	0.74	0.77
Kurtosis	2.99	1.82	1.07	0.55	0.48

835

Table 2: Nodes generated from the automatically traced fracture networks.

	SW 1	SW 2	SW 3	NE 1	NE 2
E	248	262	268	236	279
I	166	117	62	19	17
Y	4250	4390	3979	5100	2517
X	713	757	885	282	448
Penta	62	87	103	2	8
Hexa	3	9	17		
Hepta		2			

840

845 **Table 3: Average values of fracture length (m). strike (°) and sinuosity for the domains in the SW.**

	Avg. length (m)			Avg. strike (°)			Avg. sinuosity		
Gen.	SW 1	SW 2	SW 3	SW 1	SW 2	SW 3	SW 1	SW 2	SW 3
1	3.06	7.98	3.06	105.78	111.94	117.41	1.00	1.00	1.00
2	4.31	4.67	3.09	100.71	104.99	108.58	1.00	1.00	1.00
3	1.12	1.25	1.30	82.83	79.34	78.21	1.02	1.01	1.08
4	1.17	2.27	2.09	59.83	60.05	59.41	1.00	1.00	1.00
5	0.22	0.24	0.24	113.73	118.11	120.56	1.02	1.02	1.03

Table 4: Average values of fracture length (m). strike (°) and sinuosity for the domains in the NE.

	Avg. length (mm)		Avg. strike (°)		Avg. sinuosity	
Gen.	NE 1	NE 2	NE 1	NE 2	NE 1	NE 2
1	4.33	4.13	143.76	136.89	1.00	1.00
2	1.64	1.62	111.33	122.74	1.00	1.00
4	1.77	0.77	64.17	58.07	1.01	1.01
5	0.28	0.19	75.87	55.33	1.01	1.01

850

Table 5: Evolution of the fracture network in SW1.

Gen.	Avg. length (m)	Sinuosity	I	Y	X	E	Penta	Hexa
1	3.06	1.00	49	6	3	25	0	0
1 - 2	4.69	1.00	22	17	0	59	0	0
1 - 3	0.59	1.01	92	595	278	145	1	0
1 - 4	0.56	1.01	84	628	303	151	2	3
1 - 5	0.20	1.00	30	3194	849	250	96	9

Table 6: Evolution of the fracture network in SW2.

Gen.	Avg. length (m)	Sinuosity	I	Y	X	E	Penta	Hexa	Hepta	Okta
1	7.98	1.00	2	0	0	6				
1 - 2	4.51	1.00	49	10	0	49				
1 - 3	0.54	1.00	178	577	357	163	6			
1 - 4	0.50	1.00	157	612	425	173	12	4		
1 - 5	0.20	1.00	18	3057	1000	258	123	20	2	1

855

Table 7: Evolution of the fracture network in SW3.

Gen.	Avg. length (m)	Sinuosity	I	Y	X	E	Penta	Hexa	Hepta
1	3.06	1.00	48	7	2	25	0	0	0
1 - 2	3.17	1.00	52	7	2	34	0	0	0
1 - 3	0.59	1.01	203	448	262	145	8	0	0
1 - 4	0.54	1.00	179	492	329	158	15	4	0
1 - 5	0.20	1.00	12	2953	1057	275	102	16	2

860   **Table 8: Evolution of the fracture network in NE1.**

Gen.	Avg. length (m)	Sinuosity	I	Y	X	E	Penta
1	4.33	1.00	19	4		41	
1 - 2	0.79	1.00	78	65	82	54	
1 - 4	0.68	1.00	77	547	229	124	2
1 - 5	0.24	1.01	8	4135	705	283	12

Table 9: Evolution of the fracture network in NE2.

Gen.	Avg. branch length [m]	Sinuosity	I	Y	X	E	Penta
1	4.13	1.00	21	24	3	131	
1 - 2	0.80	1.00	38	95	259	145	
1 - 4	0.45	1.01	25	193	347	184	2
1 - 5	0.16	1.00	7	1888	681	230	5

865

870

875 **Table 10: Differences of the fracture networks from manual and automatic tracing.**

	SW 1	SW 2	SW 3	NE 1	NE 2
Avg. branch length (m)	0.03	0.03	0.03	0.09	-0.05
I	-136	-99	-50	-11	-10
Y	-1056	-1333	-1026	-965	-629
X	136	243	172	423	233
Penta	34	36	-1	10	-3
Hexa	6	11	-1	0	0
Hepta	0	0	2	0	0
Okta	0	1	0	0	0